

Multivariate analysis of CO₂, H₂S and CH₄ diffuse degassing and correlation with fault systems in Agua Caliente - Tzitzio, Michoacán, México

M.P. Jácome-Paz ^{a,*}, I.A. González-Romo ^a, R.M. Prol-Ledesma ^{a,d}, M.A. Torres Vera ^b, D. Pérez-Zárate ^c, A.A. Rodríguez-Díaz ^a, A.M. Estrada-Murillo ^a

^a Departamento de Recursos Naturales, Instituto de Geofísica, Universidad Nacional Autónoma de México, Circuito interior s/n, Coyoacán, 04510 Ciudad de México, México

^b Posgrado en Ciencias de la Tierra, Universidad Nacional Autónoma de México, UNAM, México

^c CONACYT-Instituto de Geofísica, Universidad Nacional Autónoma de México, Circuito interior s/n, Coyoacán, 04510 Ciudad de México, México

^d Centro Mexicano de Innovación en Energía Geotérmica (CeMIE-Geo), Carretera Tijuana-Ensenada 3919, Zona Playitas, 22860 Ensenada, B.C., México



ARTICLE INFO

Article history:

Received 28 June 2019

Received in revised form 3 February 2020

Accepted 3 February 2020

Available online 6 February 2020

Keywords:

Geothermal springs

CO₂-H₂S-CH₄ degassing

Fluid geochemistry

Agua Caliente - Tzitzio

Exploratory data analysis

ABSTRACT

The quantitative relationships between soil gas flux anomalies and faults systems in Agua Caliente-Tzitzio geothermal system were analyzed statistically. The main degassing features are related with thermal springs. The data used in the multivariate analysis are geothermal gas fluxes and spatial structural data (i.e., local fault strike). Exploratory Data Analysis (EDA) and Multivariate Analysis of Variance (MANOVA) were implemented, for the first time, to statistically describe the relation between the location of degassing features and the presence of some local fault systems, discriminating the direction of the main discharge channels and pointing to higher permeability faults. The results show that there is a statistically significant correlation between diffuse degassing of CO₂ and CH₄ and the N-S and E-W fault systems. Conversely, H₂S degassing does not show any correlation with the fault systems, which may be related with the higher H₂S reactivity compared with that of CO₂ and CH₄. It is highly recommended to use EDA and MANOVA techniques in order to establish the main degassing directions in geothermal and volcanic areas.

© 2020 Elsevier B.V. All rights reserved.

1. Introduction

Studies of diffuse degassing are fundamental to understand and to study volcanic and geothermal systems (e.g., Allard et al., 1991; Farrar et al., 1995; Giannanco et al., 1998; Gerlach et al., 1998; Hernandez et al., 2001a, 2001b; Etiope and Martinelli, 2002; Notsu et al., 2006; Mazot and Taran, 2009; Granieri et al., 2010; Bloomberg et al., 2012; Inguaggiato et al., 2012a, 2012b, 2013; Italiano et al., 2014, 2017; Ring et al., 2016; Jácome Paz et al., 2016a, 2016b; Inguaggiato et al., 2017). CO₂ is the main component of diffuse degassing in volcanic and geothermal areas due to its low solubility in silicate melts (Baubron et al., 1991).

It has been concluded in several studies, that diffuse degassing structures (DDS; Chiodini et al., 2001) are related to local and regional faults, because faults act as barriers or conduits for fluids (e.g. Klusman, 1993; Caine et al., 1996; Giannanco et al., 1998; Baubron et al., 2002; Yuce and Ugurluoglu, 2003; Yaltirak et al., 2005; Fu et al., 2005; Yuce et al., 2010, 2014, 2017a; Granieri et al., 2010; Delgado-Granados et al.,

2011; Italiano et al., 2013; Bond et al., 2017; Tamburello et al., 2018; Pfanz et al., 2019 and references therein).

High fault density areas are lithologically heterogeneous and define structural anisotropic discontinuities in the upper crust (Caine et al., 1996). Faults are characterized by (i) displacement zone known as fault core, (ii) damaged zone as the fault growth and (iii) removed adjacent protolith rocks. According to Caine et al. (1996), the dynamics among these three elements control fluid flow within and near the fault zone.

Several research studies have been done on the structures and mechanics of faults and their relationship with fluid flow (e.g. Doglioni et al., 2011, 2013, 2014). Kurz et al. (2008) reviewed studies on the 'damage zone' with faults and fractures of Riedel structures cutting sedimentary rocks, and Sibson (2000) noted that interconnecting fault network planes act as conduits for fluid circulation. They concluded that the highest concentration of deformation bands occurs close to the main faults, favoring fluid flow within the damage zone in a direction parallel to the principal fault plane. Roberts et al. (2015) investigated surface controls on the distribution of CO₂ degassing characteristics using a large geographical and historical data set. They concluded that some CO₂ seeps are strongly governed by the flow properties of the local lithology and topography. Nevertheless, permeability and local

* Corresponding author at: Departamento de Recursos Naturales, Instituto de Geofísica, Universidad Nacional Autónoma de México, Circuito interior s/n, Coyoacán, 04510 Ciudad de México, México.

E-mail address: jacome@igeofisica.unam.mx (M.P. Jácome-Paz).

faulting (Yuce et al., 2017a; D'Alessandro et al., 2018) govern some CO₂ seeps. CO₂ vents typically occur along faults in rocks that are located above the water table or have low permeability. Diffuse seeps develop where CO₂ (laterally supplied by these faults) emerges from the vadose zone and where CO₂ degassing from groundwater follows a different path due to flow differences for water and CO₂ gas. Bubbling water seeps arise where CO₂ supply enters the phreatic zone or an aquifer (Yuce and Taskiran, 2013; Yuce et al., 2017b).

The relation between faults and gas discharge has always been evaluated qualitatively; recently, Lamberti et al. (2019) used CO₂ flux field data and structural information to define the relation between gas flow and faults by overlying degassing and fault trace maps. Nonetheless, quantitative relations can be calculated by applying multivariate analysis to a set of continuous variables that include the CO₂, H₂S and CH₄ fluxes and incorporating in this analysis the presence/absence and the specific strike of the local fault systems as categorical variables. Therefore, based on implemented techniques to investigate the correlation between fluids and DDS in geothermal and volcanic areas, this work proposes the use of exploratory data analysis as a new tool for diffuse degassing data analysis. We want to highlight that the analysis will

be done for the three studied gases and not only for CO₂ flux, as it has been usually presented in the literature. In addition, it is important to note that this kind of analysis can be implemented in all zones with presence of diffuse degassing and not only in active geothermal/volcanic zones. In areas without active volcanic or hydrothermal manifestations, gas discharge may be present as normal respiration in soils (mainly represented by CO₂ degassing due to biogenic processes and degassing of cortical rocks) and this statistical analysis can be implemented to reveal the relation with some fault systems.

The objectives of this study are (i) to make distribution maps of CO₂, H₂S and CH₄ fluxes in this area, (ii) to calculate the total contribution of diffuse degassing in the area and (iii) to investigate the correlation between local faults and the spatial structure of CO₂, H₂S and CH₄ diffuse degassing.

2. Overview of study area

The study area is located 30 km southeast of the city of Morelia in Michoacán State, eastern México, and 2 km from the nearest town called Tzitzio (Fig. 1). It is in the limits of the physiographic province

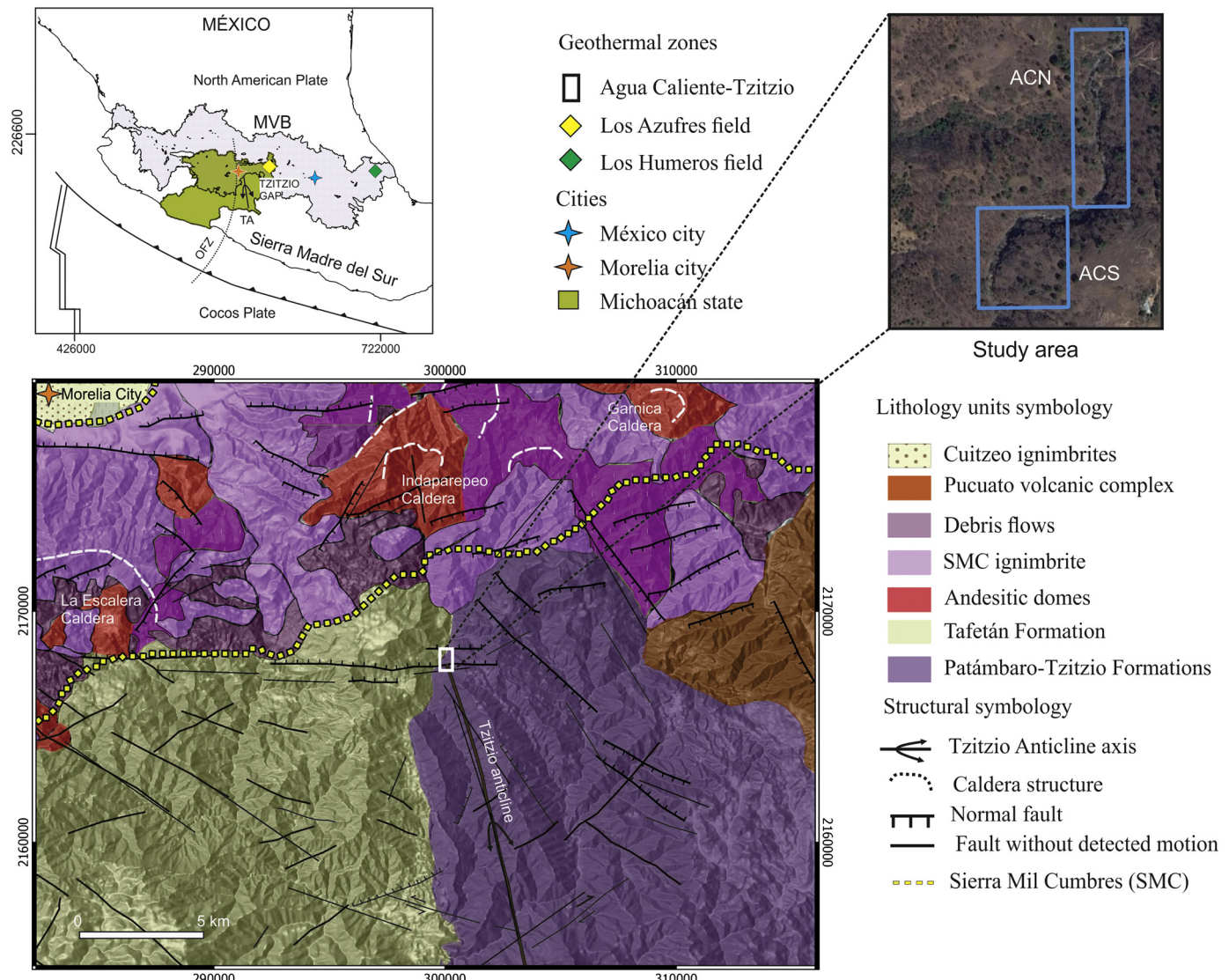


Fig. 1. Regional map of the Mexican volcanic belt (MVB), Michoacán state and Tzitzio Gap. Location of Agua Caliente Tzitzio hot springs. The study area is divided in Agua Caliente Northern (ACN) and Agua Caliente Southern (ACS). Main structural features are distinguished between faults with and without detected movement (modified of Jácome-Paz et al., 2019). Main geological units are indicated following Gómez-Vasconcelos et al., 2015; faults without detected motion and normal faults are indicated following Garduño-Monroy et al., 2009 and Morelia-E14, mineral geological chart (1998).

of the Mexican Volcanic Belt (MVB) and sub-province of Sierra Mil Cumbres composed of volcanic and pyroclastic rocks of Miocene age (Gómez-Vasconcelos et al., 2015).

The MVB is a continental arc that shows variation in its composition and tectonic regime. This arc evolved from the Neogen to the Quaternary, because of the subduction of the Cocos Plate and the Rivera microplate under the North American plate (Ferrari et al., 2012). Two main fracture zones are located to the southwest of the MVB: the Rivera fracture zone (RFZ) and the Orozco fracture zone (OFZ), the latter delimiting segments with different ages and densities of the Cocos Plate (Blatter and Hammersley, 2010).

The OFZ is a major feature of the subduction Cocos slab that has been continuously subducting beneath the overriding North American Plate under the zone of the Tzitzio Gap (TG) (Blatter and Hammersley, 2010). The denomination TG is due to the lack of active volcanism in the area, although there are several volcanic features from Early Oligocene to Middle Miocene in the margins of the TG (Pasquare et al., 1991; Morán-Zenteno et al., 2007; Blatter and Hammersley, 2010).

The study area is located at the end of the Tzitzio anticline trace (Fig. 1), which is the result of Laramide folds and thrusts that occurred during late Pliocene with an NNW-SSE trend (Gómez-Vasconcelos et al., 2015). Four regional fault systems affect the area: the old NW-SE and N-S; NE-SW; and the recent E-W (Garduño-Monroy et al., 2009). Jácome-Paz et al. (2019) concluded that the hydrothermal system of Agua Caliente - Tzitzio is controlled by the interaction of the Tzitzio Anticline with the intersections of NE-SW and E-W normal faults related to the intra-arc extension of the MVB.

There are two Eocene units of the Tzitzio Formation that outline the study area (Pasquare et al., 1991): a) conglomerate and b) sandstone. The conglomerate is polymictic, matrix-supported and poorly sorted consisting of milky subangular quartz clasts with a variable size of 0.5–5 cm, sub-rounded andesite clasts of 1–7 cm, clasts of metamorphic rocks with size between 1 and 4 cm, and occasionally limestone clasts <3 cm within a sandstone matrix (30%). A fine-grained sandstone with moderate oxidation presenting reddish colors overlies the conglomerate. Thermal discharge occurs through the conglomerate that has a porosity of approximately 8%, estimated from petrographic observations (Pérez-Zárate et al., 2017).

2.1. Previous degassing studies

In 2017, Jácome-Paz et al. (2019) reported CO₂ fluxes with a minimum value of 3 g m⁻² d⁻¹, a maximum value of 29,484 g m⁻² d⁻¹ and a mean value of 1427 g m⁻² d⁻¹ in the Agua Caliente north area (ACN). According with the GSA method, the total data set was divided in two degassing groups: the low flux group was represented by 70% of the values (group A) and the high flux group was represented by 30% of the data (group B). The total CO₂ diffuse flux obtained was 0.15 ton d⁻¹. There were some locations closer to the main thermal spring and on bubbling zones (~20% of data set) that show CH₄ degassing. The range of CH₄ flux values was within 2.2 to 5.3 g m⁻² d⁻¹.

On Agua Caliente South area (ACS), the obtained CO₂ flux had a minimum value of <1 g m⁻² d⁻¹, a maximum value of 1925 g m⁻² d⁻¹ and a mean value of 227 g m⁻² d⁻¹. The GSA method shows two degassing groups: the low flux group represents 80% of the data (group A) and the high flux group represents 20% of the data (group B). The total CO₂ diffuse flux was 0.17 ton d⁻¹. Some locations close to the main warm spring and on intensely bubbling areas (~30% of total measured data) present CH₄ degassing with values within 4.8 to 20.6 g m⁻² d⁻¹.

In both zones, there was no diffuse emission of H₂S within the detection range of the sensor.

3. Materials and methods

3.1. Field geology and structural measurements

The studied area is divided in Agua Caliente North (ACN) and Agua Caliente South (ACS) (Fig. 1). Basic field exploration, including geology and diffuse emission measurements, was carried out at local level in ACN and ACS. The geological exploration consisted in the identification of main fault characteristics. Structural measurements were collected at two sites located along the river where thermal springs occur. Fieldwork included both qualitative and quantitative analyses of fault structural data (orientation, dimension, spatial distributions, fault type and spacing) in the outcrops of the sedimentary sequence. Mapping of lithology, structural data and hydrothermal alteration was integrated in a Geographic Information System (QGIS®); additionally, the structural data were plotted in Stereonet® to identify the main fault systems.

3.2. Soil gas flux determinations

A new soil CO₂ flux survey at Agua Caliente-Tzitzio thermal springs was performed on February 2018, during dry season and under stable atmospheric pressure. Soil flux measurements were performed following the accumulation chamber method using a West Systems fluxmeter (Chiodini et al., 1998). Gas flux on the water surface (thermal springs, bubbling pools and water bubbling pools) was measured following the method proposed by Bernard and Mazot (2004).

In both cases, soil and water, the fluxmeter had the following sensors: (Allard et al., 1991) LICOR LI-800, a nondispersive infrared CO₂ sensor with detection range of 0.1 to 20,000 ppm, accuracy of <3% and reproducibility below 10% for the range 0.2 to 10,000 g m⁻² d⁻¹; (Baubron et al., 1991) CH₄-WS infrared, which has a flux detection range from 0.02 to 1444 g m⁻² d⁻¹, 5% accuracy, 2% of repeatability, 22 ppm resolution and $\pm 25\%$ precision for the range 0.1–5 mol m⁻² d⁻¹ and $\pm 10\%$ precision for the range 5–150 mol m⁻² d⁻¹; and (Baubron et al., 2002) WEST H₂S-BH chemical detector, which has a flux detection range from 0.2×10^{-3} to 0.6 mol m⁻² d⁻¹, accuracy of 3%, factory calibration of 20 ppm and zero offset ≤ 0.2 ppm. Due to the rate of consumption of the detector, the H₂S flux is systematically 10% underestimated in the accumulation chamber A and 5% underestimated in the accumulation chamber B. In addition, the H₂S detector is affected by interference sensitivity for several species (SO₂, NO, NO₂, Cl₂, H₂, C₂H₄, CO, NH₃); therefore, low fluxes can be interpreted to be the result of the interference sensitivity effect (West Systems, 2012).

Flux Revision software of the West system, Wingslib®, Surfer® and Origin® software were used for flux data post-processing. The graphical statistical approach method (GSA) and sequential Gaussian simulation (SGSIM) were performed to compute the total CO₂ flux (Sichel, 1966; Sinclair, 1974; Chiodini et al., 1998; Deutsch and Journel, 1998; Cardellini et al., 2003). The GSA method permits differentiation among different CO₂ degassing groups or families (e.g. Jácome Paz et al., 2016a, 2016b). Usually these groups can be related with degassing mechanisms: (i) low flux values may be associated with background or soil respiration and (ii) anomalously high values of fluxes with hydrothermal input. The SGSIM technique allows to calculate the total flux and to describe main degassing alignments showing the spatial distribution of fluxes. All distribution maps were done with Gaussian simulation, using a grid of 5 × 5 m and with 100 simulations for each area. The total covered areas of each zone were computed using both, GPS coordinates and Wingslib® software.

3.3. Exploratory data analysis

The hypothesis of this paper is that gas anomalies generally occur as linear, fault linked-features, as well as in irregularly shaped diffuse or halo anomalies and irregularly spaced plumes or spot anomalies.

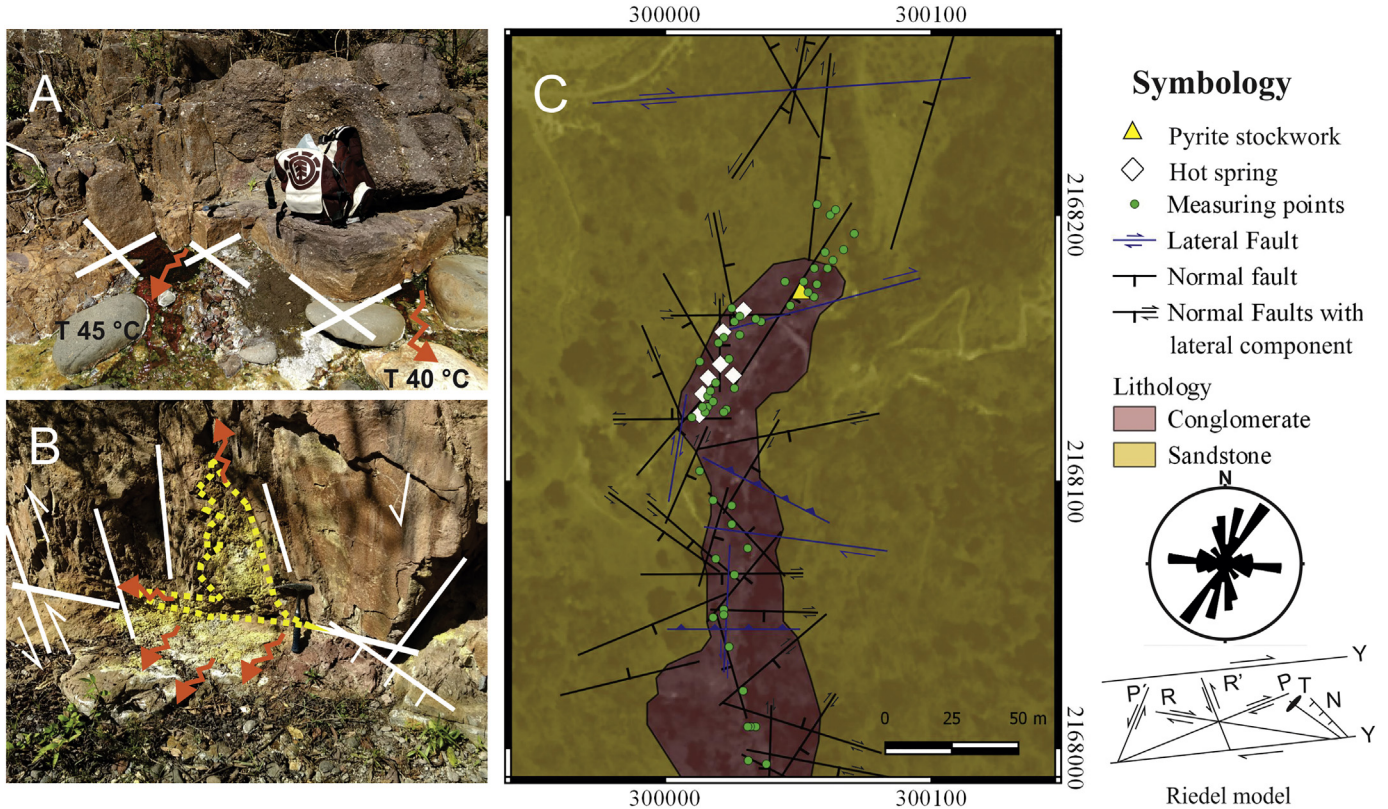


Fig. 2. Field photos of the hot spring sites and associated faults. Detailed map of the hot springs of ACN. (A) Photo of a fault network, with the structural assemblage composed of normal faults and thermal discharges. The white lines indicate the fault trace of Riedel network. Arrows indicate direction of discharge. (B) Network of Riedel structures within structurally influenced hydrothermal flow. Yellow dotted lines indicate halo of alteration and arrows indicate direction of flow (C) Structural settings for ACN and location of measuring points of diffuse degassing. Main hot springs observed on field are reported.

Therefore, spatial gas flux patterns in faulted areas appear to be suitable tools for identifying these features. Geostatistical techniques were applied to the study of spatially correlated data, as described below.

Exploratory data analysis (EDA) performs an examination of the data to suggest partial descriptions and hidden relationships, regardless of the statistical criteria used in confirmatory settings. EDA is an approach to analyze data sets and summarize their main characteristics, often with graphic methods that include descriptive statistics. One of the most important objectives of geospatial data EDA is to characterize the range of spatial autocorrelation that is exhibited by the data. The graphic results of EDA are presented as box and variance plots that provide a qualitative evaluation of the correlation among variables (Tukey, 1977; Davis, 2002).

Data processing was performed with MANOVA for the 3 continuous variables that represent the gas flux of CO_2 , H_2S and CH_4 , and two categorical variables: fault system strike and the degassing groups (A and B). MANOVA analyzes the relationship between the variables (gas flux) and co-variables represented by degassing groups (A and B) and fault system strikes by comparing the mean value and the covariance structure of the data among the dependent and independent variables.

The result of this comparison yields the correlation coefficient and the p -value, which represents the statistical significance of the results: the smaller the p -value, the greater the statistical significance. In Earth Sciences, the convention is that a p -value lower than 0.05 is considered as evidence that the mean values differences are statistically significant. The evaluation of the results was done using Wilks criterion. In MANOVA tests there are differences between group means for a combination of dependent variables. Wilks Criterion is a measure of the percent variance in dependent variables not explained by differences in levels of the independent variable. A p -value of zero means that there is no variance that is not explained by the independent variables (Wilks, 1932); therefore, a p -value equal to zero is expected if the

variance of the dependent variable is totally explained by the variance of the independent variables. The p -value measures the probability that the studied hypothesis is true, or the probability that the data were produced by random chance, in this case the correlation between degassing and the presence of faults. A small p -value means that there is strong evidence that a statistical test is valid. The maximum value to consider a hypothesis to be true is 0.05 (Gibbons and Pratt, 1975).

Data processing included the collected data of the diffuse emissions of CH_4 , CO_2 and H_2S in $[\text{g m}^{-2} \text{d}^{-1}]$ units. Information on the presence/absence and direction of the faults was included numerically as categorical variables with the same spatial coordinates as the diffuse emission variables. The fault variables were classified in four types: (0) no faults, (Allard et al., 1991) ORT fault system, which includes N-S and W-E fault systems, (Baubron et al., 1991) NW-SE fault system and (Baubron et al., 2002) NE-SW fault system. An additional variable with information about the degassing groups A and B was also included in the analysis (see Appendix A). The location of both, flow data and faults, was expressed in UTM coordinates (14 north) and spatial reference system WGS 1984. Collected data were processed with the software: Statistica 10.0 (StatSoft Inc.).

4. Results

4.1. Geological description

4.1.1. Agua Caliente North (ACN)

Surface hydrothermal manifestations are represented by several hot springs with $\text{Na}-\text{HCO}_3$ water type (<50 °C, Jácome-Paz et al., 2019) and diffuse emanations of gas (Jácome-Paz et al., 2019 and this work) at the crossing of faults with trend NW-SE and E-W. In the surroundings of the springs there is argillic hydrothermal alteration with clay minerals like kaolinite and halloysite in <50 cm halos, deposits of red crusts of

schwertmannite $[Fe^{3+}O_{16}(OH)_{12}(SO_4)_2]$ and stockwork veins of opal, quartz and pyrite (Jácome-Paz et al., 2019).

The sedimentary rock outcrops along the NNE-SSW river section show faults, tensile fractures, joints and veinlets. This zone presents intense faulting, the four regional fault systems are reflected locally (NW-SE, N-S, NE-SW and E-W, Fig. 2) with the presence of the right-lateral strike-slip normal faults, normal with right and left lateral components, and inverse faults. Fault structures are still well preserved and recognizable even with a low fracture density. Window sampling method was used for assessing fracture variability, density and intensity on conglomerate unit outcrops (e.g. Priest, 1993; Zeeb et al., 2013). Rectangular window sampling (4×2 m) records a total of 110 measurements, fractures with an interval of length from 0.05 to 3.5 m, an average density of $5 (m^{-2})$ with a variation between 4 and $10 (m^{-2})$, and an average intensity of $6.5 (m \times m^{-2})$ in a range of 4 to $11 (m \times m^{-2})$.

These structures are characterized by a main slip plane that is striated and polished, and occasionally has associated abrasive slickensides. The striations and orientations of the slickensides, where present, are consistent with a predominantly normal slip, with right- or left-lateral slip components depending on local surfaces. In these structures, the fault core is very thin and poorly developed, a few millimeters thick or single fault planes, and the damage zone consists of <8 cm wide fracture zone. In general, there is no evidence of circulation of thermal fluids through the main faults (e.g. halos of alteration), but associated faults show laminated veinlets (<1 cm) of opal and quartz filling normal, predominantly, and strike-slip faults, also tensile fractures present hydrothermal alteration.

The structures form an association of faults and fractures that intersect and reach each other in a network-like arrangement. The fault network has ~ 2 m wide and occasionally replicates every ~ 20 m along the west edge of the river. Inside each fault network, the crosscutting and

contact relationships among the fractures, faults and striated slip surfaces suggest that these structures belong to the same deformation event. Interconnecting fault planes provide a conduit for fluid circulation. The argillic alteration develops in halos (<50 cm), mainly crosscutting or in the contact between faults. Occasionally, opal and quartz veinlets (<1 cm) can be observed.

The structural analysis shows that the fault distribution and type agree with a Riedel-type model (Riedel, 1929), where the master fault is of lateral type that generates and/or intersects normal faults (N) and normal faults with lateral component (R' and P' faults), in addition to inverse faults. The identified Riedel systems consist of N70–85°E master right lateral faults (Y), related to: (a) N65–75°E right lateral faults P, (b) N06–12°E normal faults with left lateral component P', (c) N10–20°W normal faults with lateral component R', and (d) N20–34°E fractures and normal faults T (Fig. 2).

The hydrothermal discharge is related to the systems of faults and fractures P, P', R', and T types.

4.1.2. Agua Caliente South (ACS)

In the southern area there are two main thermal springs (<52 °C, Jácome-Paz et al., 2019) located at the intersection of NW and E-W faults, and a cold spring discharge on the trace of the N64°E fault (Fig. 3). The hydrothermal alteration present is analogous to that of the northern portion: kaolinite, halloysite, schwertmannite and pyrite, having wider distribution and higher intensity than in the northern area.

Structurally, it presents faulting similar to the north zone, with the presence of normal faults with right and left lateral components. The results evaluated for the second network of natural fractures, with rectangular window sampling of 4×2 m show fracture lengths between 0.05 and 3.8 m, a lower average density of fractures $4.4 (m^{-2})$, with a

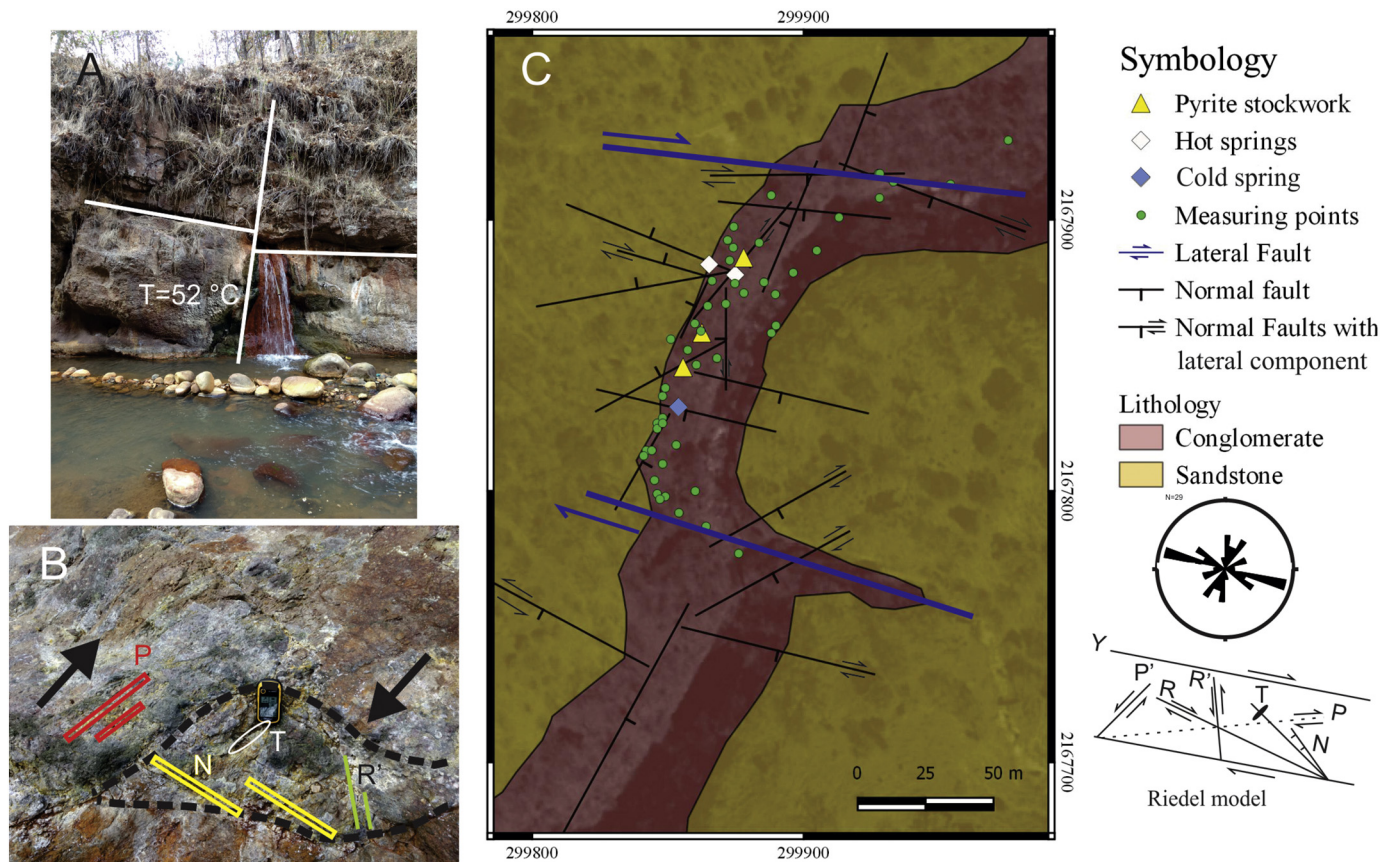


Fig. 3. Field photos of the (A) hot spring at the intersection of fault and stratification of conglomerate. (B) Photo of a fault network, with the structural assemblage composed of faults type P, N, T and R'. (C) Structural settings for ACS and location of measuring points of diffuse degassing.

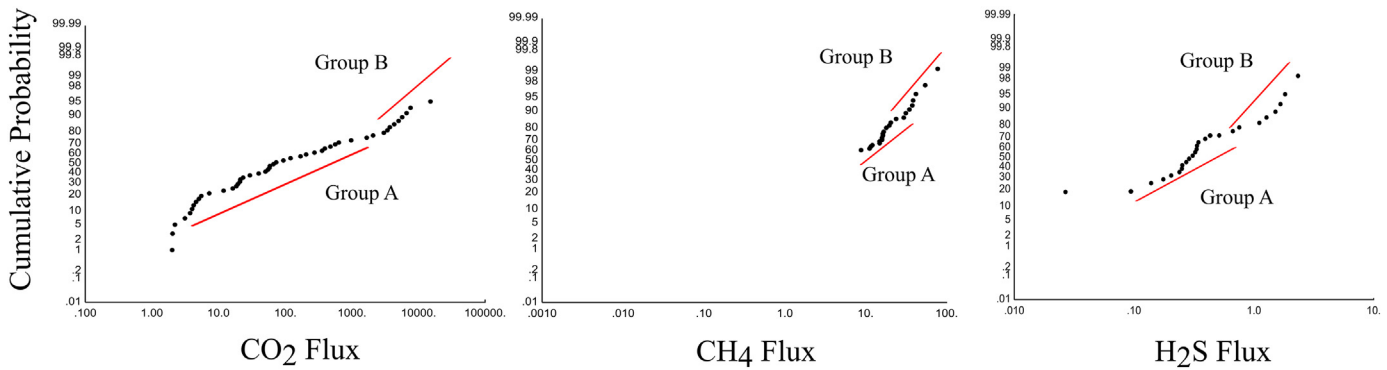


Fig. 4. Cumulative probability plot for CO_2 , CH_4 and H_2S fluxes on ACN. Two degassing groups were inferred by GSA method in each measured gas.

variation between 4 and 9 (m^{-2}) and an average intensity of 5.8 ($\text{m} \times \text{m}^{-2}$) in a range between 4 and 10 ($\text{m} \times \text{m}^{-2}$), with respect to ACN. The Riedel system in this section is composed of the N70–84°W master faults, associated with: (a) N50–60°E left lateral faults P', (b) N55–70°W normal faults with right side component R, (c) N4–10°W normal fault with left side component R', (d) N10–20°W normal faults N, and (e) N56–60°E fractures and normal faults T with orientation (Fig. 3).

The intersection of P', R, R', N, and T faults and fractures types control the occurrence of hydrothermal discharges.

4.2. Diffuse degassing

4.2.1. Agua Caliente North (ACN)

Some 57 points of fluxes with a CO_2 flux minimum value of $\sim 0 \text{ g m}^{-2} \text{ d}^{-1}$, maximum value of $181,764 \text{ g m}^{-2} \text{ d}^{-1}$ and mean value of $6675 \text{ g m}^{-2} \text{ d}^{-1}$ were measured in ACN area.

The GSA method, through cumulative probability plot for the total data set of CO_2 flux, shows two degassing groups: the low values group (A) represented by 80% of the data set with a maximum flux value of $1614 \text{ g m}^{-2} \text{ d}^{-1}$ and the high values group (B) represented by 20% of the data corresponding to the values measured at bubbling zones and with maximum value of $\sim 181,764 \text{ g m}^{-2} \text{ d}^{-1}$ (Fig. 4). After Gaussian simulation, the mean value (corresponding with bubbling zones) was $2829 \text{ g m}^{-2} \text{ d}^{-1}$. The model was a spherical variogram with sill 1 and nugget of 0.2. The grid was done with $5 \times 5 \text{ m}$ cell covering an area of $25,200 \text{ m}^2$. The total CO_2 diffuse flux obtained by SGSIM was 71.29 ton d^{-1} (Table 1).

There were some locations closer to the main thermal spring and on bubbling zones that show CH_4 degassing. The range of measured CH_4 flux is within 0 – $78 \text{ g m}^{-2} \text{ d}^{-1}$. The mean flux was $10.7 \text{ g m}^{-2} \text{ d}^{-1}$. The GSA method shows two degassing families: the low values group (A) represented by 85% of the data set with a maximum flux value of $2.04 \text{ g m}^{-2} \text{ d}^{-1}$ and the high values group (B) represented by 15% of the data with maximum value of $\sim 78 \text{ g m}^{-2} \text{ d}^{-1}$. After Gaussian simulation, the mean value, without outliers, was $1.8 \text{ g m}^{-2} \text{ d}^{-1}$. The model was a spherical variogram with sill 1.1 and nugget of 0.6. The grid was done with $5 \times 5 \text{ m}$ cell covering an area of $25,200 \text{ m}^2$. The total CH_4 flux obtained by SGSIM was 0.04 ton d^{-1} .

There were some locations closer to the main thermal spring with visible alteration of pyrite and significant values of H_2S flux. The range of measured H_2S flux values is within 0 – $2.7 \text{ g m}^{-2} \text{ d}^{-1}$. The GSA method

shows two degassing families: the low values group (A) represented by 70% of the data set with a maximum flux value of $0.310 \text{ g m}^{-2} \text{ d}^{-1}$ and the high values group (B) represented by 30% of the data with maximum value of $2.7 \text{ g m}^{-2} \text{ d}^{-1}$. After Gaussian simulation, the mean value of H_2S was $0.3 \text{ g m}^{-2} \text{ d}^{-1}$. The model was a spherical variogram with sill 1 and nugget of 0.4. The grid was done with $5 \times 5 \text{ m}$ cell covering an area of $25,200 \text{ m}^2$. The total H_2S flux obtained by SGSIM was 0.007 ton d^{-1} .

The obtained distribution maps (Fig. 5) of the three gases show some spatial patterns. Three different maps were made for the three gases, by changing the scale to identify some spatial patterns in the degassing features. In the case of CO_2 flux, the ranges are 0 – $1000 \text{ g m}^{-2} \text{ d}^{-1}$, 1000 – $10,000 \text{ g m}^{-2} \text{ d}^{-1}$ and all values 0 – $190,000 \text{ g m}^{-2} \text{ d}^{-1}$. High degassing values were observed in the intersection of faults (northern of ACN area, corresponding with the hot springs location verified in the field) and low CO_2 fluxes were observed in NE-SW tending faults. The presence of active faults controls the CO_2 diffusion, which is influenced by both the pH value and the hydrolysis of silicates such as plagioclase generating the $\text{Na}-\text{HCO}_3$ water type as reported by Jácome-Paz et al. (2019). Thermal springs have between 6.2 and 6.6 pH, while river water downstream of thermal springs and upstream of thermal springs has 7–8.6 pH respectively, (Jácome-Paz et al., 2019).

In the case of H_2S the ranges where 0 – $0.5 \text{ g m}^{-2} \text{ d}^{-1}$, 0.5 – $2.750 \text{ g m}^{-2} \text{ d}^{-1}$ and all values 0 – $2.750 \text{ g m}^{-2} \text{ d}^{-1}$. High values seem to be divided by the W-E alignment in the central part of the zone allowing major degassing of H_2S in the northern part of ACN area across hot springs and their surroundings. Main H_2S degassing was detected along NW-SE and NE-SW directions that correlate with pyrite deposits and main hot springs.

The ranges of 0 – $10 \text{ g m}^{-2} \text{ d}^{-1}$, 10 – $80 \text{ g m}^{-2} \text{ d}^{-1}$ are characteristic of CH_4 distribution maps. The behavior of this gas is like H_2S degassing with high values in the northern part of the area around main hot springs location and, additionally, a small zone in the southern part which corresponds with a minor bubbling zone. CH_4 flux seems to be dominated by NW-SE and W-E directions.

4.2.2. Agua Caliente South (ACS)

Some 49 points were measured in ACS area. CO_2 flux minimum value of $2.5 \text{ g m}^{-2} \text{ d}^{-1}$, a maximum value of $27,000 \text{ g m}^{-2} \text{ d}^{-1}$ and a mean value of $3217 \text{ g m}^{-2} \text{ d}^{-1}$ were obtained. The cumulative probability plot for the total data set shows two degassing groups: the low flux

Table 1

CO_2 fluxes values obtained with GSA and SGSIM techniques for ACN area.

	Group (%)	Mean value GSA technique ($\text{g m}^{-2} \text{ d}^{-1}$)	Mean value GSIM technique ($\text{g m}^{-2} \text{ d}^{-1}$)	Total SGSIM CO_2 flux (ton d^{-1}) area: $25,200 \text{ m}^2$
Group A	80	276	2829	
Group B	20	33,512		
Total flux				71

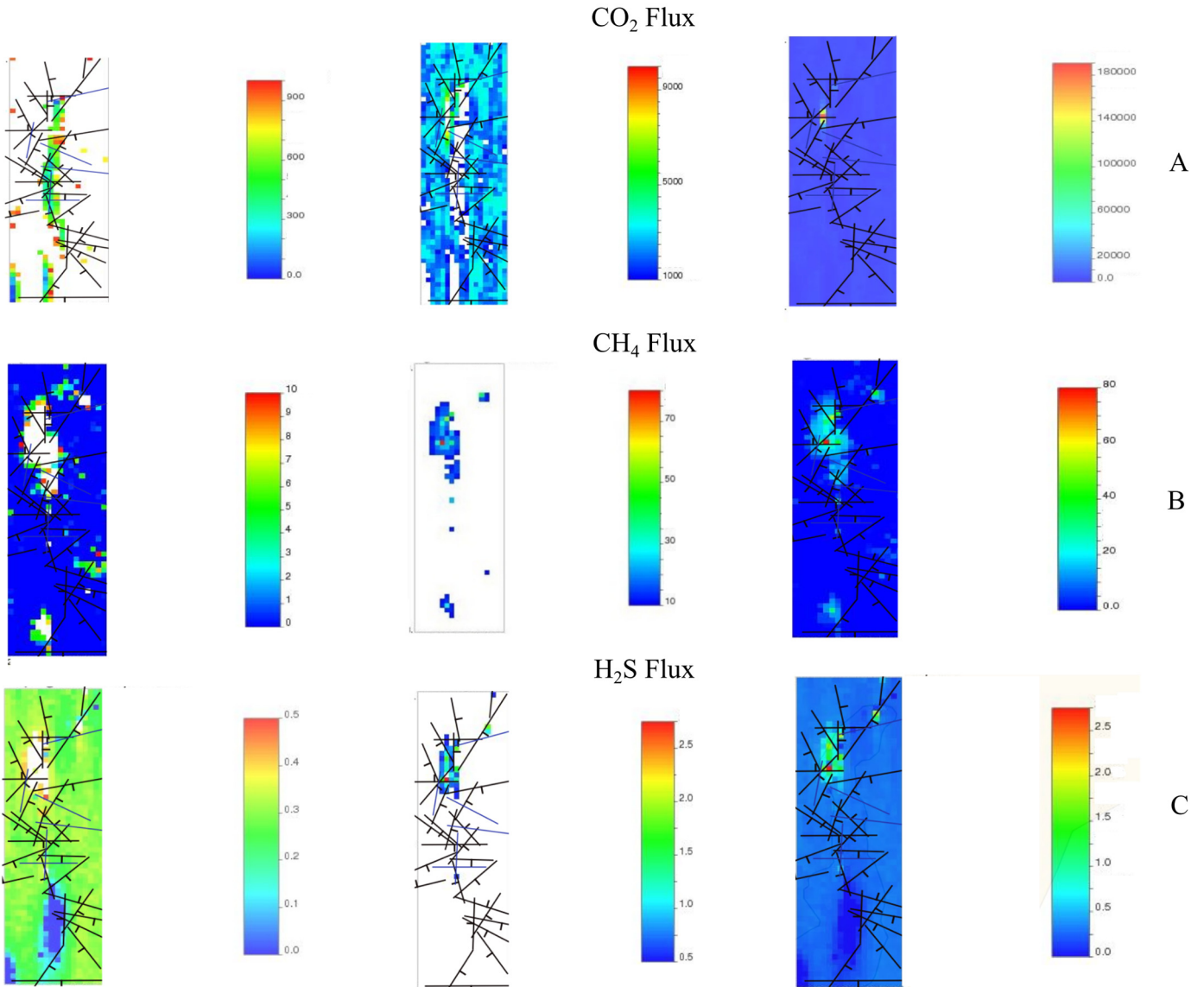


Fig. 5. Distribution maps were overlaid on local structural features reported on this study. All color scales are presented in $\text{g m}^{-2} \text{d}^{-1}$ unit. Different ranges of fluxes were used for each figure to highlight possible alignments and spatial patterns. (A) CO_2 fluxes. Left to right: 0–1000; 1000–10,000 and 0–190,000 $\text{g m}^{-2} \text{d}^{-1}$. (B) CH_4 fluxes. Left to right: 0–10, 10–80 and 0–80 $\text{g m}^{-2} \text{d}^{-1}$. (C) H_2S fluxes. Left to right: 0–0.5, 0.5–2.750 and 0–2.750 $\text{g m}^{-2} \text{d}^{-1}$.

group (A) represented by 90% of the data set with maximum value of $36.45 \text{ g m}^{-2} \text{d}^{-1}$ and the high values (group B) was represented by 10% of the data with a maximum value of $27,000 \text{ g m}^{-2} \text{d}^{-1}$ (Fig. 6). After Gaussian simulation, the mean value without the outliers was $105 \text{ g m}^{-2} \text{d}^{-1}$. The model was a spherical variogram with sill 1 and

nugget of 0.2. The grid was done with $5 \times 5 \text{ m}$ cells covering an area of $23,200 \text{ m}^2$. The total CO_2 diffuse flux obtained by SGSIM was 2.43 ton d^{-1} (Table 2).

There were some locations close to the main thermal spring and on bubbling zones that show CH_4 degassing. The range of measured CH_4

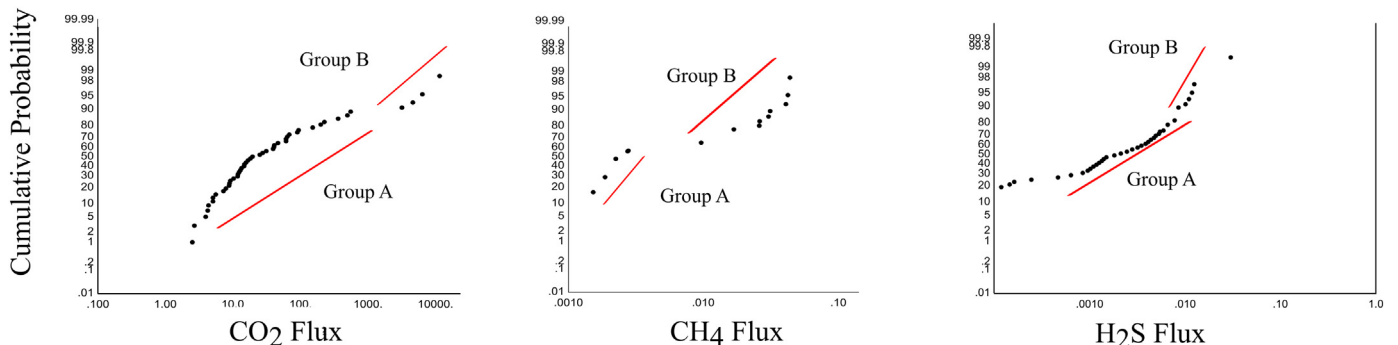


Fig. 6. Cumulative probability plot for CO_2 , CH_4 and H_2S fluxes on ACS. Two degassing groups were inferred by GSA method in each measured gas.

Table 2CO₂ fluxes values obtained with GSA and SGSM techniques for ACS area.

Group (%)	Mean value GSA technique (g m ⁻² d ⁻¹)	Mean value SGSM technique (g m ⁻² d ⁻¹)	Total SGSM CO ₂ flux (ton d ⁻¹) Area: 23,200 m ²
Group A	90	20.9	105
Group B	10	5294	
Total flux			2.5

flux values is within 0–30 g m⁻² d⁻¹. The GSA method shows two degassing families: the low values group (A) represented by 60% of the data set with a maximum flux value of 0.2608 g m⁻² d⁻¹ and the high values group (B) represented by 40% of the data with maximum value of 30 g m⁻² d⁻¹. After Gaussian simulation, the mean value, without outliers, was 0.04 g m⁻² d⁻¹. The model was a spherical variogram with sill 1.2 and nugget of 0.15. The grid was done with 5 × 5 m cell covering an area of 23,200 m². The total CH₄ diffuse flux obtained by SGSM was 0.0009 ton d⁻¹.

There were some locations with significant values of H₂S fluxes. The range of measured H₂S flux values is within 0–0.2 g m⁻² d⁻¹. The GSA method shows two degassing families of fluxes: the low values group (A) represented by 90% of the data set with a maximum flux value of 0.0999 g m⁻² d⁻¹ and the high values group (B) represented by 10%

of the data with maximum value of 0.2 g m⁻² d⁻¹. After Gaussian simulation, the mean value of H₂S was 0.04 g m⁻² d⁻¹. The model was a spherical variogram with sill 1 and nugget of 0.3. The grid was done with 5 × 5 m cell covering an area of 23,200 m². The total H₂S diffuse flux obtained by SGSM was 0.0001 ton d⁻¹.

The obtained distribution maps of the three gases (Fig. 7) show some spatial structures. Three different maps were made, one for each gas, changing the scale of discharge values to visualize the possible spatial structure in the degassing values. In the case of CO₂, the ranges are 0–400, 0–1000 and all values 0–28,000 g m⁻² d⁻¹. Main degassing can be observed in the trace of NE-SW direction (western part of ACS area, corresponding with the location of the main hot spring as reported in Jácome-Paz et al., 2019 and verified in the field). In the case of H₂S the ranges where 0–0.05, 0–0.2 and all values 0–4 g m⁻² d⁻¹. High H₂S

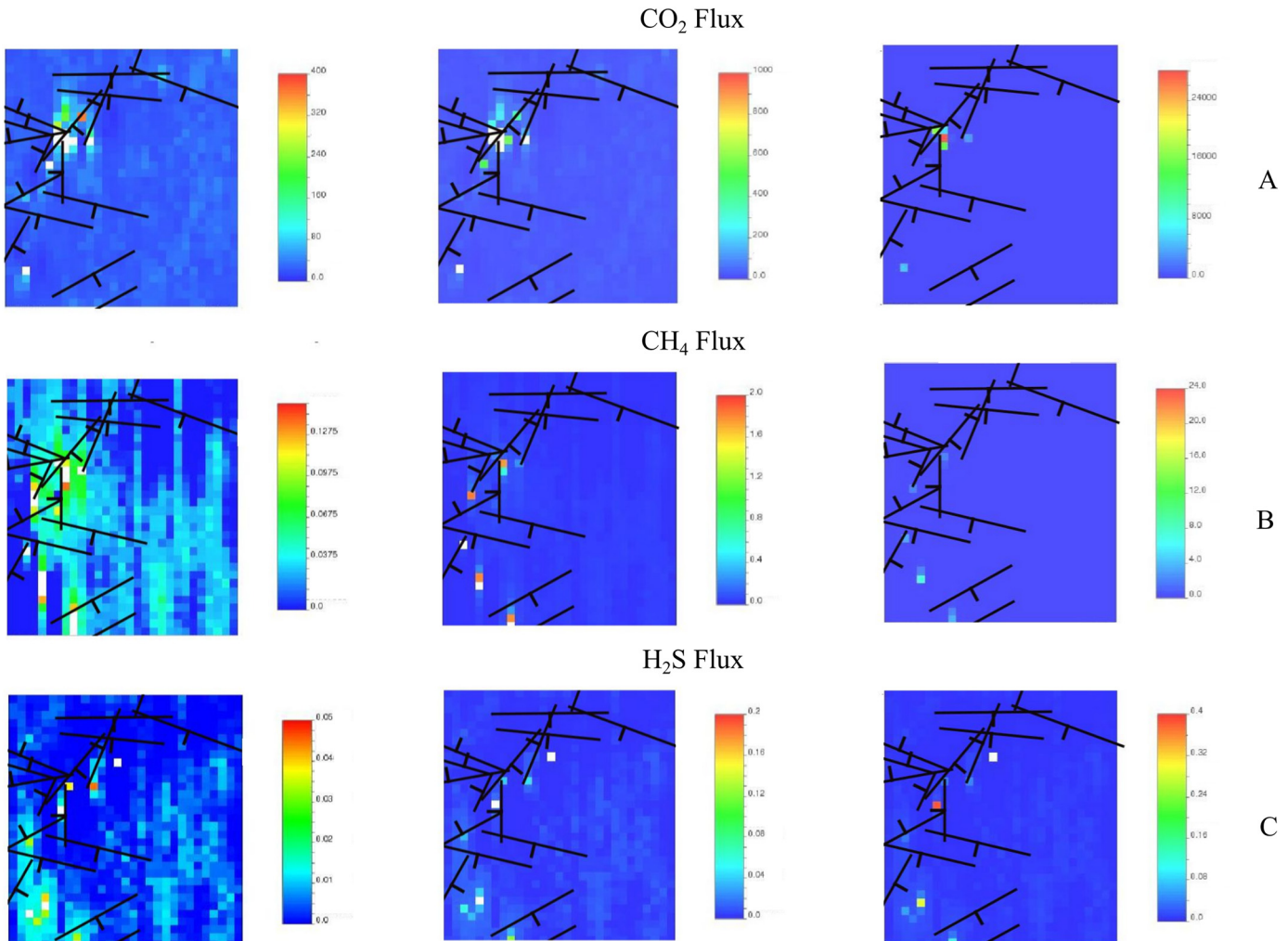


Fig. 7. Distribution maps were overlaid with local structural features reported in this study. All color scales are presented in g m⁻² d⁻¹ unit. For each figure, different ranges of fluxes were used to highlight possible alignments and spatial patterns. (A) CO₂ fluxes. Left to right: 0–400; 0–1000 and 0–28,000 g m⁻² d⁻¹. (B) CH₄ fluxes. Left to right: 0–0.15; 0–2 and 0–0.24 g m⁻² d⁻¹. (C) H₂S fluxes. Left to right: 0–0.05; 0–0.2 and 0–4 g m⁻² d⁻¹.

Table 3

Descriptive statistics of CO_2 , CH_4 and H_2S degassing data used for EDA analysis. All flux values are in $\text{g m}^{-2} \text{ d}^{-1}$ unit.

Variable	Valid N	Mean	Median	Minimum	Maximum	Std. dev.
CO_2	2082	2797.43	525	34.68	181,764.0	7978.75
CH_4	1991	1.09	0.03	0.0	78.0	4.52
H_2S	949	0.004	0.06	0.0	0.3	0.01

fluxes are reported at the same locations, where pyrite deposits can be observed and across the same direction as CO_2 discharge. For the CH_4 distribution maps, the observed ranges are $0\text{--}0.15 \text{ g m}^{-2} \text{ d}^{-1}$; $0\text{--}2 \text{ g m}^{-2} \text{ d}^{-1}$ and all values are within the interval $0\text{--}24 \text{ g m}^{-2} \text{ d}^{-1}$. The highest flux values are located directly on the main hot springs area.

4.3. Exploration data analysis

EDA results show that CH_4 and H_2S flux values have low dispersion, as highlighted by the low value of the variation coefficient (Std. Dev.). Otherwise, the wide ranges, as well as the high skewness values for CO_2 , indicate the presence of statistical outliers. (Table 3).

Box plots are used to display and compare qualitatively the distribution of the gas data set with those related with faults with different orientation (Figs. 8, 9, 10). The plots indicate that the mean CO_2 flux value is similar for all fault system directions, but there are some high values that may be considered as statistical outliers; however, they are reliable data that provide valuable information on intense CO_2 degassing (Fig. 8). In the case of CH_4 and H_2S , the mean values are similar in all directions as well as the standard deviation; therefore, there are no statistical outliers (Figs. 9, 10). The MANOVA results (Table 4) show that there is a statistically significant correlation ($p < 0.05$) between diffuse degassing of CO_2 and CH_4 and the presence of faults.

Figs. 11 and 12 show that degassing is mostly correlated with the ORT system (N-S and E-W fault systems). Conversely, H_2S degassing does not show a statistically significant correlation ($p = 0.341$) with any of the fault systems (Table 4).

Figs. 13, 14 and 15 are variance plots that show that degassing group A (background soil degassing) consistently has the lowest values for all fault systems, independently of the fault direction. The highest gas flux of the B degassing group, which is linked to the anomalous geothermal gas flux, are associated with the ORT fault system and the lowest values correspond to the no fault group. MANOVA results (Table 5) show that there is a statistically

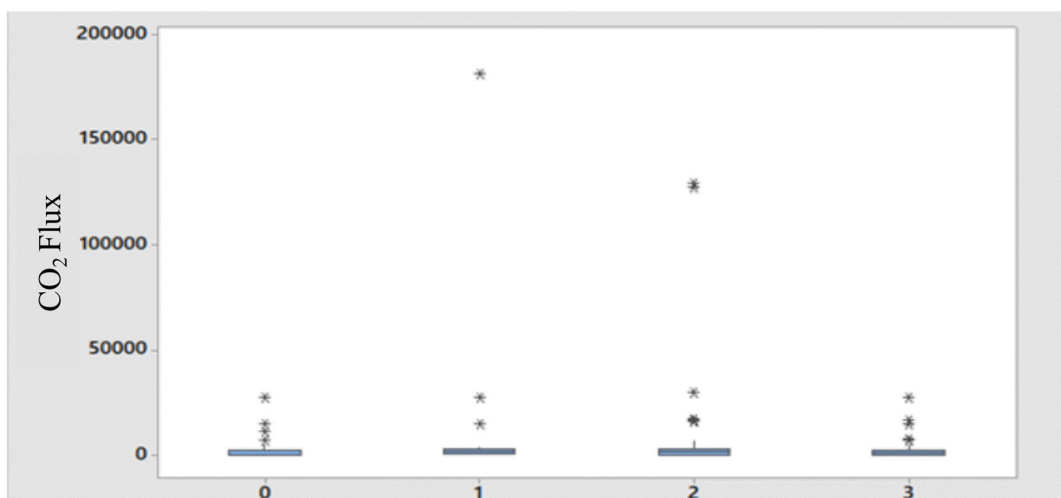


Fig. 8. Boxplot of the CO_2 diffuse flux data, where 0 - no faults, 1 - ORT fault system, which includes N - S and W - E faults, 2 - NW - SE faults and 3 - NE - SW faults.

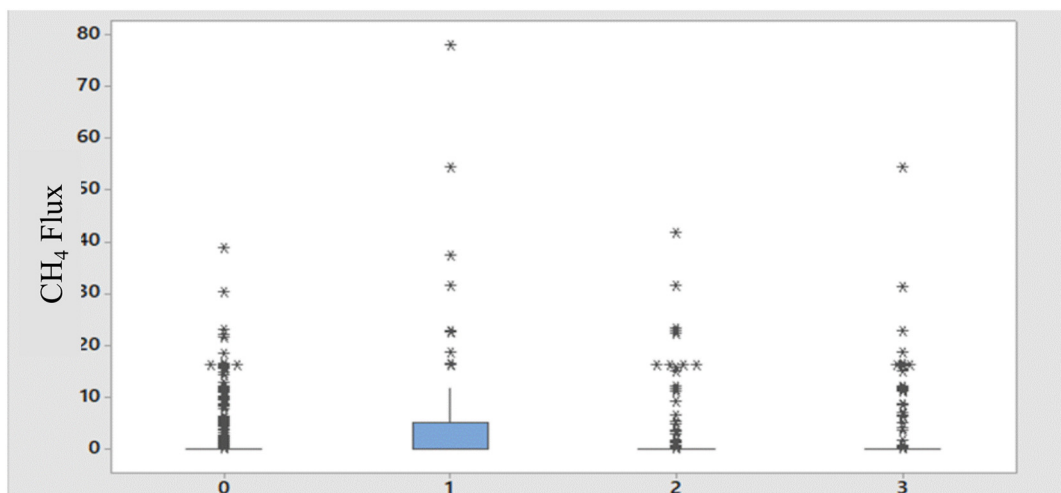


Fig. 9. Boxplot of the CH_4 diffuse flux data, where 0 - no faults, 1 - ORT fault system, which includes N - S and W - E faults, 2 - NW - SE faults and 3 - NE - SW faults.

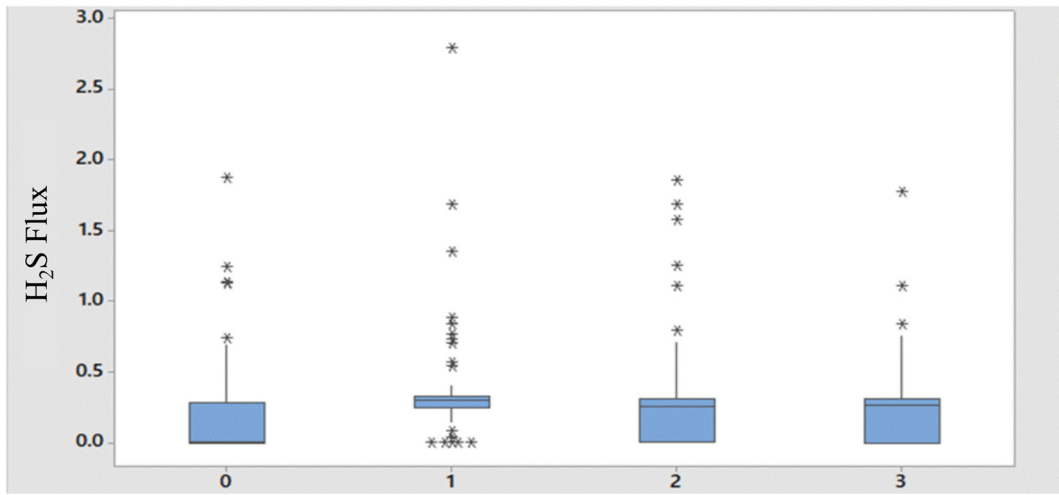


Fig. 10. Boxplot of the H₂S diffuse flux data, where 0 - no faults, 1- ORT fault system, which includes N - S and W - E faults, 2 - NW - SE faults and 3 - NE - SW faults.

Table 4

MANOVA results: Wilks' Criterion correlation analysis of gas flux and faults presence.

Wilks' criterion		
Gas flux	Correlation coef	p-Value
CO ₂	0.985	0.000
CH ₄	0.947	0.000
H ₂ S	0.996	0.341

significant correlation for CO₂, CH₄ and H₂S ($p < 0.05$) with diffuse degassing groups (A and B) according to GSA method.

5. Discussion

In this work, geostatistical analysis was performed to investigate the presence of phenomena acting along specific directions (e.g., fault-related anisotropy effect). Recent works observed a relation of anomalous gas concentrations with active faults and confirmed that the gas discharge is a deep fault indicator (Ciotoli et al., 1998, 1999, 2005; Lombardi et al., 1996; Klusman, 1993; Zhiguan, 1991; Baubron et al., 2002). Active faults favor gas flow because they generally increase rock and soil permeability, thus the presence of linear soil gas anomalies

longer than several meters is often taken as strong evidence of tectonic features (Ciotoli et al., 1998; Fridman, 1990). It is important to note that faults have typically wide fracture zones that can also be crosscut by other structures, thus resulting in diffuse or "halo" anomalies (Matthews, 1985; Sokolov, 1971).

The structural survey performed throughout the river with thermal discharges has defined a Riedel system along two principle trends, one almost E-W and the other with a NW direction (Figs. 2 and 3), which agree with the regional trends observed throughout Tzitzio anticlinal and Mil Cumbres (Gómez-Vasconcelos et al., 2015; Jácome-Paz et al., 2019). At the surface, the intersection of major faults, with their associated Riedel type fractures and faults, forms openings (<2 cm opening) in the compact conglomerate unit that hosts them, providing a highly permeable pathway for the hydrothermal discharges to escape toward the surface. Degassing related to faults can be either 'direct leak anomalies' where the gas measured corresponds to the deep gas phase or 'secondary anomalies' linked to the geological characteristics of the fault (Baubron et al., 2002); according to Jácome-Paz et al. (2019) the isotope value of carbon (CO₂) in gas samples (bubbling zones) is -5.7‰ δC13 PDB for ACN and -5.9‰ δC13 PDB for ACS, indicating a magmatic origin in both zones. Because of that, we propose a model (Fig. 16) for ACN and ACS, where faults going deep correspond to those defining bubbling zones (and thermal spring manifestations) in surface, and

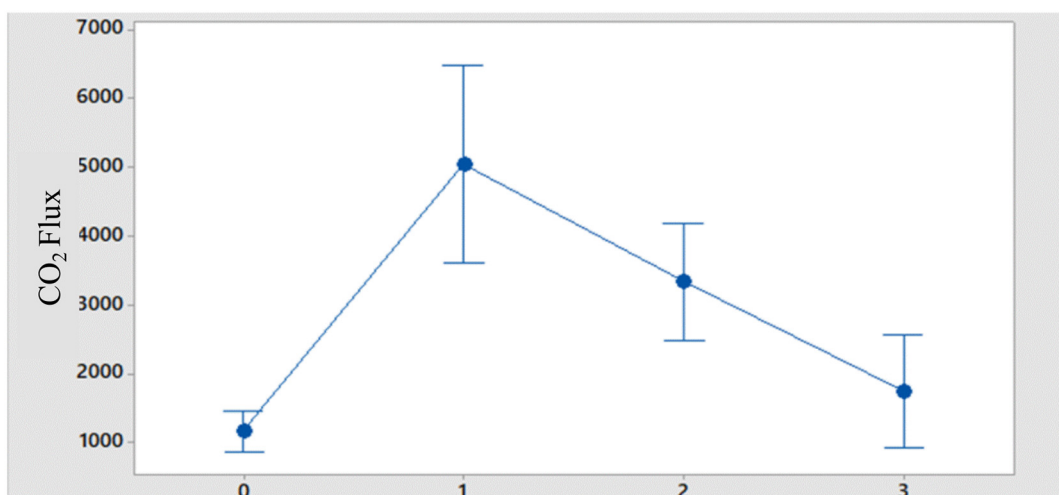


Fig. 11. Variance plot of the CO₂ diffuse flux data, where 0 - no faults, 1- ORT fault system, which includes N - S and W - E faults, 2 - NW - SE faults and 3 - NE - SW faults.

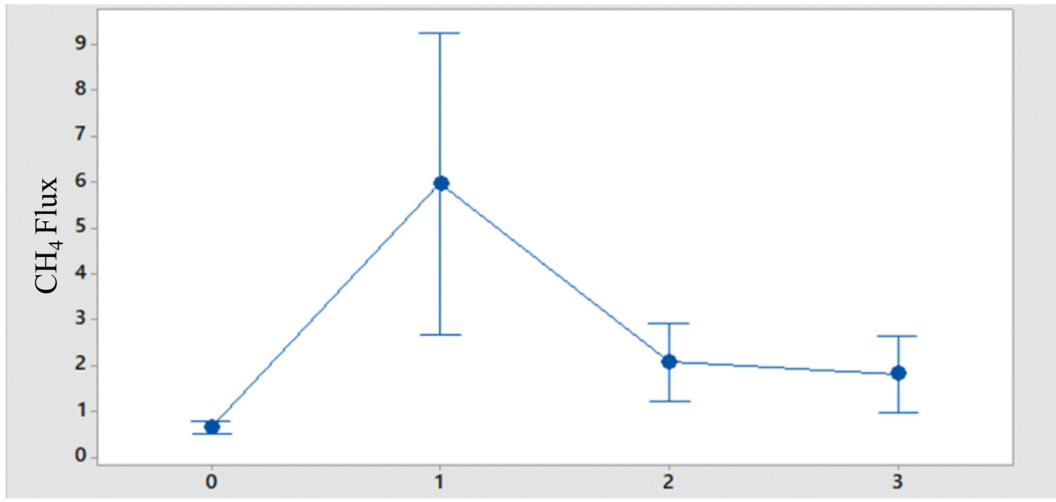


Fig. 12. Variance plot of the CH₄ diffuse flux data, where 0 - no faults, 1 - ORT fault system, which includes N - S and W - E faults, 2 - NW - SE faults and 3 - NE - SW faults.

coincidentally, all these are the master faults of the area. As this model is presented as a complement and visual tool for the statistical correlation obtained between faults strikes and degassing, two different and unique depths are assumed for the master faults and for the remaining faults. The illustrative depth that allows contact with deeper layers and a possible thermal reservoir was chosen for the master faults that allow the degassing to rise. Determining the depth of the failures goes beyond the scope of this article.

Similarly to what has been observed in other areas, where gas diffusion is closely related specifically with active faults (e. g. Ciotoli et al., 1998; Fridman, 1990; Lamberti et al., 2019), the field evidence shows greater fluid flow at the intersections of the P', R', and T faults (Figs. 2

and 3), and it does not show substantial flow along major faults, consistently with the results of the statistical analysis. According to Tamburello et al. (2018) extensional tectonics and, in particular, normal and strike slip faults are the most suitable scenario for CO₂ degassing, our results are in agreement with this.

In addition, in Agua Caliente zone, the hydrothermal discharges do not occur along the entire length of any given fault but instead it is focused in small areas (Figs. 5 and 7). This implies a complex permeability distribution related to the fault system, where hydrothermal flow occurs via preferential pathways consisting of well-interconnected fault networks. According to Faulkner et al. (2010) flow can be dominated by a small number of fractures within the surrounding damage zone

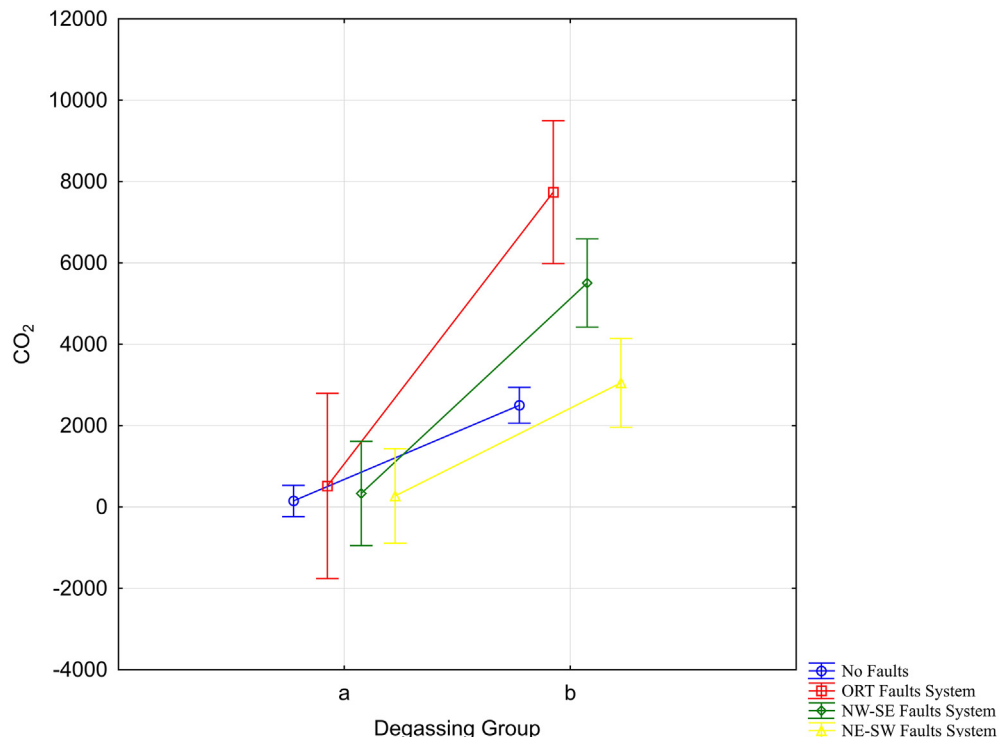


Fig. 13. Variance plot of the CO₂ diffuse flux data assembled by degassing group. Group A represents the background soil degassing and group B represents the anomalous geothermal degassing. $F = 6.3327$, $p = 0.00029$. Vertical bars denote 0.95 confidence intervals.

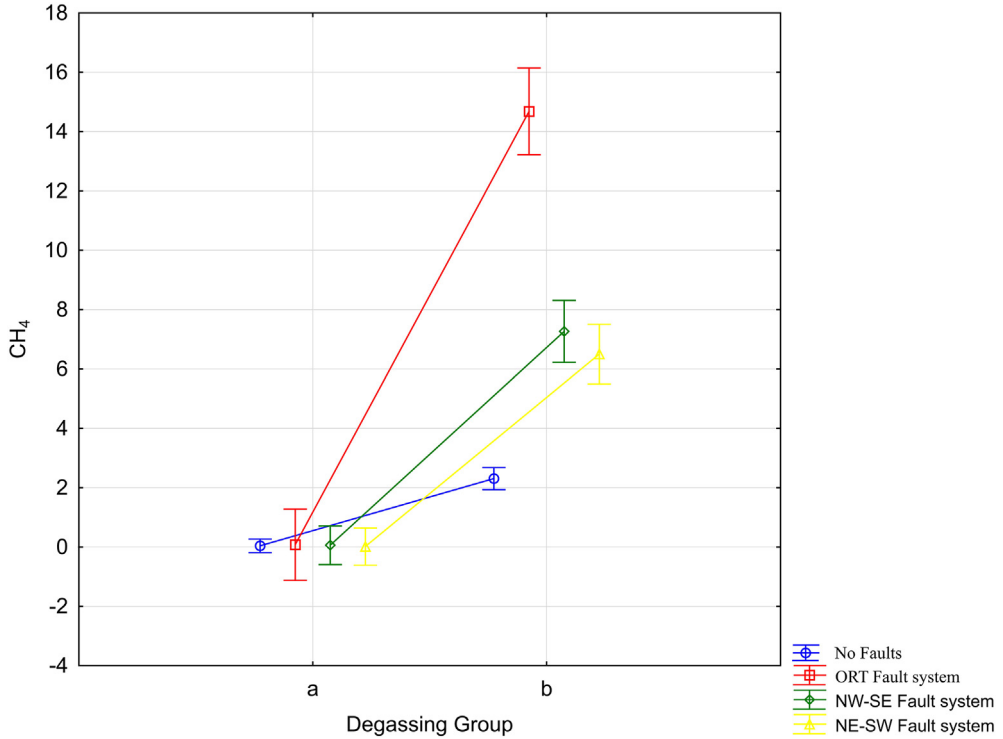


Fig. 14. Variance plot of the CH_4 diffuse flux data assembled by degassing group. Group A represents the background soil degassing and group B represents the anomalous geothermal degassing. $F = 12.063$, $p = 0.00000$. Vertical bars denote 0.95 confidence intervals.

in the fault systems and the complex structure in a fault, fundamental role in CO_2 propagation by creating pathways extending from the deep crust to the earth surface.

Regarding the preferential degassing direction (named as DDS, diffuse degassing structures by Chiodini et al., 2001), in Agua Caliente it

is observed that the ORT fault system is correlated with the highest anomalous values (Family B) of gas flux for CO_2 and CH_4 ; therefore, it is very likely that the ORT fault system is more active in comparison with the NW-SE and NE-SW fault systems. In the case of H_2S , the lack of correlation with any fault system is possibly associated with higher

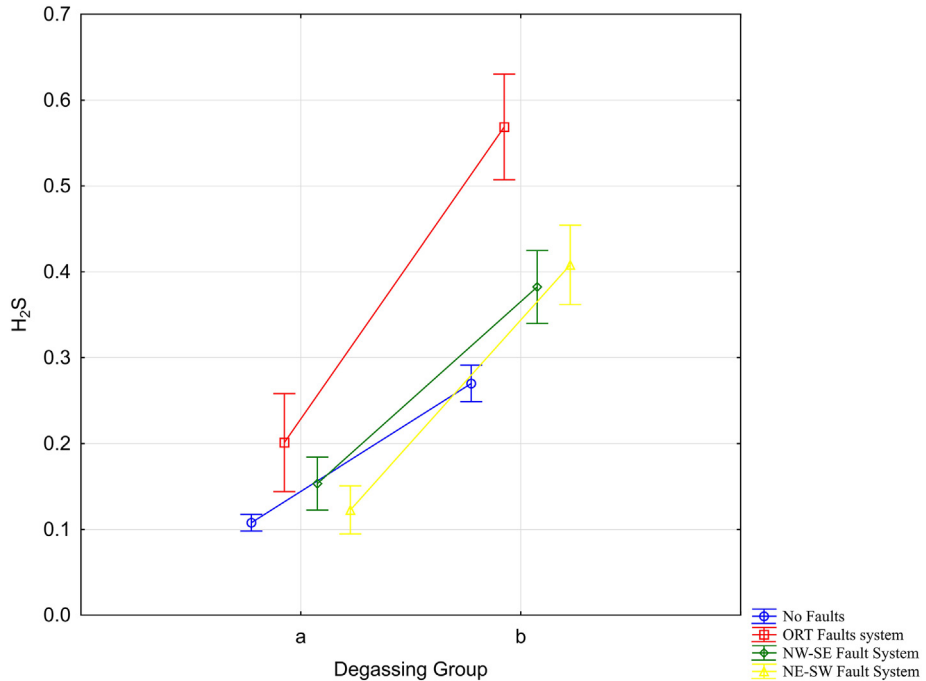


Fig. 15. Variance plot of the H_2S diffuse flux data assembled by degassing group. Group A represents the background soil degassing and group B represents the anomalous geothermal degassing. $F = 12.063$, $p = 0.000$. Vertical bars denote 0.95 confidence intervals.

Table 5

MANOVA results: Wilks' Criterion correlation analysis of gas flux and degassing groups (A and B for all gases).

Wilks' criterion		
Gas flux	Correlation coef	p-Value
CO ₂	0.979	0.000
CH ₄	0.792	0.000
H ₂ S	0.873	0.000

H₂S reactivity compared with that of CO₂ and CH₄; that produces abundant pyrite deposition observed in the surface manifestations and affected the total H₂S flow measured.

6. Concluding remarks

Gas release at the surface is not continuous along strike-slip faults; instead, it occurs at specific NW and NE trends due to channeled flow along more permeable pathways along the P', R', and T faults. Work at Agua Caliente-Tzitzio thermal zone fault shows a clear link between deformation style, secondary permeability characteristics, and the spatial distribution and flux rates of deep gas to the surface.

EDA and MANOVA were implemented, for the first time, to statistically describe the relation between the location of degassing features and the presence of some local fault systems, discriminating the direction of the main discharge channels and pointing to higher permeability faults.

EDA and MANOVA are well-established methods that would be valuable in basic geothermal exploration to define correlations between local structural settings and diffuse degassing on soils that may be useful to infer permeable structures to be considered for exploitation planning. Local structural geology, which usually is well described as part of the basic exploration of a geothermal area, must be known for this kind of study. If possible, a more complete data set of structural parameters should be used after reconnaissance exploration.

It is highly recommended to use EDA and MANOVA techniques in order to establish the main degassing directions in geothermal and volcanic areas.

Spatial correlation methods allow, as shown in the present work, to validate the statistical significance of the correlation between fault systems and gas discharge in the studied area. There is an obvious relation between faults and permeability that allows gas discharge; however, the specific strike that favors gas flow toward the surface can be objectively determined with the multivariate statistical analysis.

A statistically significant correlation was found between ORT fault systems and CO₂ flux. The other fault systems do not present any significant correlation. According to these results, and taking [Roberts et al. \(2015\)](#) classification, the CO₂ seeps at Agua Caliente – Tzitzio occur along faults in rocks that are located above the water table or have low permeability. This configuration allows CO₂ diffuse seeps to be laterally supplied by the local faults and, in this case, bubbling CO₂ occurs due to the presence of the river and the hot springs. Thermal springs discharge at the surface and CO₂ diffuse degassing follow a similar flow path.

Author statement

Mariana Patricia Jácome Paz, fieldwork, conceptualization, methodology, writing original draft.

Irving Antonio Gonzalez Romo, fieldwork, conceptualization and methodology.

Rosa María Prol Ledesma, project administration, resources, validation, conceptualization.

Marco Antonio Torres Vera, conceptualization, methodology, review.

Daniel Pérez Zárate, fieldwork, methodology, review.

Augusto Rodríguez, fieldwork, methodology, review.

Aurora Estrada Murillo, fieldwork, methodology.

Data availability

Datasets related to this article are available and can be requested to the corresponding author.

Declaration of competing interest

All authors declare that they have no financial and personal relationship with other persons or organizations that may improperly influence (skew) their work or state if there are no interests to declare.

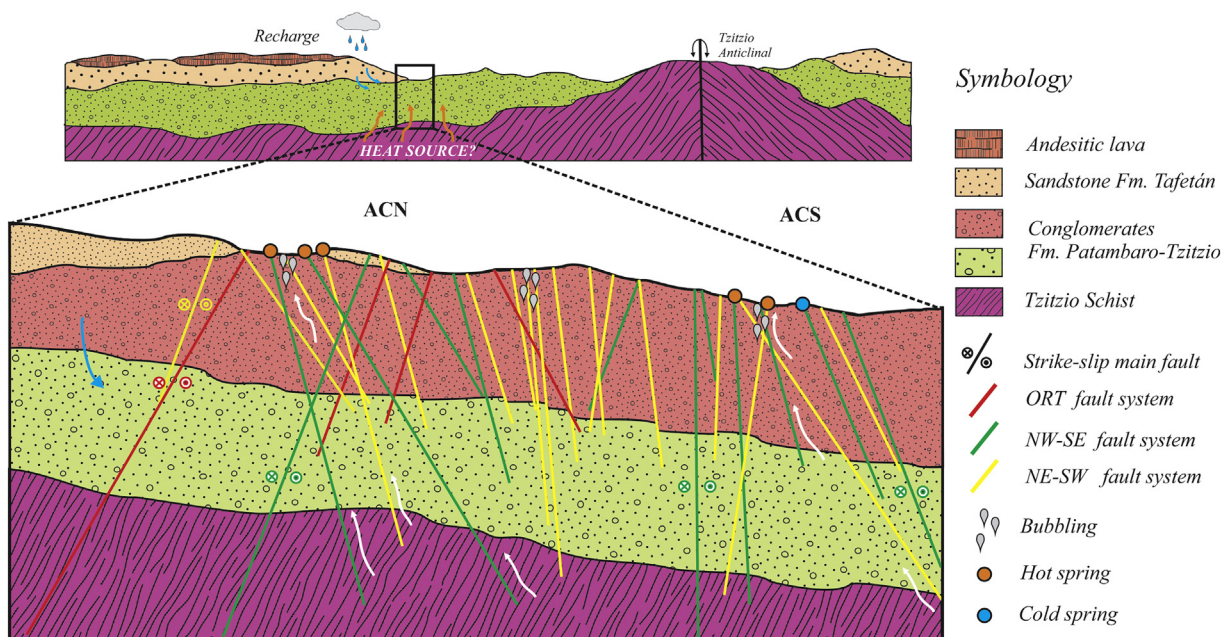


Fig. 16. Conceptual model of degassing in Agua Caliente (North and South) zone. The deepest failures allude to the master failures of the area. The ACS NW-SE fault whose surface feature is characterized by the exit of the cold springs on the surface is sufficiently deep to let the groundwater in the area rise.

Acknowledgments

This work was financially supported by the Mexican Center for Innovation in Geothermal Energy, CeMIE Geo. Grant number 207032 CONACyT/SENER, through Project P01 "Mapas de gradiente geotérmico y flujo de calor para la república mexicana". The authors wish to thank Juan Luis Carrillo de la Cruz for his help in processing data. The authors thank the comments by two anonymous reviewers that greatly improved the original manuscript and editor Prof. Alessandro Aiuppa.

Appendix A. Supplementary data

Supplementary data to this article can be found online at <https://doi.org/10.1016/j.jvolgeores.2020.106808>.

References

- Allard, P., Carbonelle, J., Dajlevic, D., Le Bronec, J., Morel, P., Robe, M.C., Maurenas, J.M., Faivre-Pierret, R., Martins, D., Sabroux, J.C., Zettwoog, P., 1991. *Eruptive and diffuse emissions of CO₂ from Mount Etna*. *Nature* 351, 387–391.
- Baubron, J.C., Allard, P., Toutain, J.P., 1991. Diffuse volcanic emission of carbon dioxide from Volcano Island, Italy. *Nature* 344, 51–53. <https://doi.org/10.1038/344051a0>.
- Baubron, J.C., Rigo, A., Toutain, J.P., 2002. Soil gas profiles as a tool to characterize active tectonic areas: the Jaut Pass example (Pyrenees, France). *Earth and Planet Science Letters* 196, 69–81. [https://doi.org/10.1016/S0012-821X\(01\)00596-9](https://doi.org/10.1016/S0012-821X(01)00596-9).
- Bernard, A., Mazot, A., 2004. Geochemical evolution of the young crater lake of Kelud volcano in Indonesia. In: Wanty, Seal, I.I. (Eds.), *Water-Rock Interaction* (WRI-11). Balkema Publishers, p. 4.
- Blatter, D., Hammersley, L., 2010. Impact of the Orozco Fracture Zone on the central Mexican Volcanic Belt. *J. Volcanol. Geotherm. Res.* 197, 67–84.
- Bloomberg, S., Rissmann, C., Mazot, A., Oze, C., Horton, T., Gravley, D., Pawson, J., 2012. Soil gas flux exploration at the Rotokawa geothermal field and White Island, New Zealand. *Proceedings, Thirty-Sixth Workshop on Geothermal Reservoir Engineering*.
- Bond, C.E., Kremer, Y., Johnson, G., Hicks, N., Lister, R., Jones, D.G., Haszeldine, R.S., Saunders, I., Gilfillan, S.M.V., Shipton, Z.K., Pearce, J., 2017. The physical characteristics of a CO₂ seeping fault: the implications of fracture permeability for carbon capture and storage integrity. *International Journal of Greenhouse Gas Control* 60, 49–60.
- Caine, J.S., Evans, J.P., Forster, C.B., 1996. Fault zone architecture and permeability structure. *Geology* 24, 1025–1028.
- Cardellini, C., Chiodini, G., Frondini, F., 2003. Application of stochastic simulation to CO₂ flux from soil: mapping and quantification of gas release. *J. Geophys. Res.* 108, 2425. <https://doi.org/10.1029/2002JB002165>.
- Chiodini, G., Cioni, R., Guidi, M., Raco, B., Marini, L., 1998. Soil CO₂ flux measurements in volcanic and geothermal areas. *Appl. Geochem.* 13, 543–552. [https://doi.org/10.1016/S0883-2927\(97\)00076-0](https://doi.org/10.1016/S0883-2927(97)00076-0).
- Chiodini, G., Frondini, F., Cardellini, C., Granieri, D., Marini, L., Ventura, G., 2001. CO₂ degassing and energy release at Solfatara volcano, Campi Flegrei, Italy. *J. Geophys. Res.* 106 (B8), 16,213–16,221.
- Ciotoli, G., Guerra, M., Lombardi, S., Vittori, E., 1998. Soil gas survey for tracing seismogenic faults: a case study in the Fucino Basin, central Italy. *J. Geophys. Res.* 103 (23), 781–794.
- Ciotoli, G., Etiöpe, G., Guerra, M., Lombardi, S., 1999. The detection of concealed faults in the Ofanto basin using the correlation between soil gas fracture surveys. *Tectonophysics* 299, 321–332.
- Ciotoli, G., Lombardi, S., Morandi, S., Zarlenga, F., 2005. A multidisciplinary statistical approach to study the relationships between helium leakage and neo-tectonic activity in a gas province: the Vasto Basin, Abruzzo-Molise (central Italy). *AAPG Bull.* 88 (3), 355–372.
- D'Alessandro, W., Yüce, G., Italiano, F., Bellomo, S., Gülbay, A.H., Yasin, D.U., Gagliano, A.L., 2018. Large compositional differences in the gases released from the Kizildag ophiolitic body (Turkey): evidences of prevailingly abiogenic origin. *Mar. Pet. Geol.* 89, 174–184.
- Davis, J.C., 2002. *Statistics and Data Analysis in Geology*. 3rd edn. Wiley, New York.
- Delgado-Granados, H., Espinasa-Perera, R., Rodríguez, S.R., Barrera-Morales, W., Jácome-Paz, M.P., 2011. Use of soil CO₂ flux for the recognition of the most active zones in the Xalapa Monogenetic Volcanic Field. In: Eineder, M., Brčic, R., Adam, N., Minet, C. (Eds.), *Monitoring and Observations of Active Volcanoes Using In-situ and Remote Sensing Techniques*. European Geosciences Union.
- Deutsch, C.V., Journel, A.G., 1998. *GSLIB: Geostatistical Software Library and Users Guide*. 2nd edition. Oxford University Press, New York.
- Doglioni, C., Barba, B., Carminati, E., Riguzzi, F., 2011. Role of the brittle–ductile transition on fault activation. *Phys. Earth Planet. Inter.* 184, 160–171.
- Doglioni, C., Barba, B., Carminati, E., Riguzzi, F., 2013. Fault on-off versus coseismic fluids reaction. *Geosci. Front.* <https://doi.org/10.1016/j.gsf.2013.08.004>.
- Doglioni, C., Barba, B., Carminati, E., Riguzzi, F., 2014. Fault on-off versus strain rate and earthquakes energy. *Geosci. Front.* 5 (6), 767–780. <https://doi.org/10.1016/j.gsf.2013.12.007>.
- Etiöpe, G., Martinelli, G., 2002. Migration of carrier and trace gases in the geosphere: an overview. *Phys. Earth Planet. Inter.* 129, 185–204.
- Farrar, C.D., Sorey, M.L., Evans, W.C., Howle, J.F., Kerr, B.D., Kennedy, B.M., King, C.Y., Southon, J.R., 1995. Forest-killing diffuse CO₂ emission at Mammoth Mountain as a sign of magmatic unrest. *Nature* 376, 675–678.
- Faulkner, D.R., Jackson, C.A.L., Lunn, R.J., Schlische, R.W., Shipton, Z.K., Wibberley, C.A.J., Withjack, M.O., 2010. A review of recent developments concerning the structure, mechanics and fluid flow properties of fault zones. *J. Struct. Geol.* 32 (11), 1557–1575.
- Ferrari, L., Orozco-Esquível, T., Manea, V., Manea, M., 2012. The dynamic history of the Trans-Mexican Volcanic Belt and the Mexico subduction zone. *Tectonophysics* 522–523, 122–149.
- Fridman, A.I., 1990. Application of naturally occurring gases as geochemical pathfinders in prospecting for endogenetic deposits. *J. Geochem. Explor.* 38, 1–11.
- Fu, C.C., Yang, T.F., Walia, V., Chen, C.H., 2005. Reconnaissance of soil gas composition over the buried fault and fracture zone in southern Taiwan. *Geochem. J.* 39, 427–439. <https://doi.org/10.2343/geochemj.39.427>.
- Garduño-Monroy, V.H., Pérez-López, R., Israde-Alcántara, I., Rodríguez-Pascua, M.A., Szynkaruk, E., Hernández-Madrigal, V.M., García-Zepeda, M.L., Corona-Chávez, P., Ostroumov, M., Medina-Vega, V.H., García-Estrada, G., Carranza, O., López-Granados, E.J., Mora-Chaparro, J.C., 2009. Paleoseismology of the southwestern Morelia-Acambaro fault system, central Mexico. *Geofis. Int.* 48 (3), 319–335.
- Gerlach, T.M.J., Doukals, M.P., McGee, K.A., Kessler, R., 1998. Three-year decline of magmatic CO₂ emission from soils of a Mammoth Mountain tree kill: Horseshoe Lake, CA, 1995–1997. *Geophys. Res. Lett.* 25, 1947–1950.
- Giammanco, S., Gurrieri, M., Valenza, S., 1998. Anomalous soil CO₂ degassing in relation to faults and eruptive fissures on Mount Etna (Sicily, Italy). *Bull. Volcanol.* 60, 252–259. <https://doi.org/10.1007/s00445-005-0231>.
- Gibbons, J.D., Pratt, J.W., 1975. *P-values: Interpretation and Methodology* 20–25. Am. Stat. 29–1.
- Gómez-Vasconcelos, M.G., Garduño-Monroy, V.H., Macías, J.L., Layer, P., Benowitz, J.A., 2015. *The Sierra de Mil Cumbres, Michoacán, México: transitional volcanism between the Sierra Madre Occidental and the Trans-Mexican Volcanic Belt*. *J. Volcanol. Geotherm. Res.* 301, 128–147.
- Granieri, D., Avino, R., Chiodini, G., 2010. Carbon dioxide diffuse emission from the soil: ten years of observations at Vesuvio and Campi Flegrei (Pozzuoli), and linkages with volcanic activity. *Bull. Volcanol.* 72, 103–118. <https://doi.org/10.1007/s00445-009-0304-8>.
- Hernandez, P.A., Salazar, J.M., Shimoike, Y., Mori, T., Notsu, K., Pérez, N.M., 2001a. *Diffuse emission of CO₂ from Miyakejima volcano, Japan*. *Chem. Geol.* 177, 175–185.
- Hernandez, P.A., Notsu, K., Salazar, J.M., Mori, T., Natale, G., Okada, H., Virgili, G., Shimoike, Y., Sato, M., Perez, N.M., 2001b. *Carbon dioxide degassing by advective flow from Usu volcano, Japan*. *Science* 292, 83–86.
- Inguaggiato, S., Calderone, L., Inguaggiato, C., Mazot, A., Morici, S., Vita, F., 2012a. Long-time variation of soil CO₂ fluxes at summit crater of Vulcano (Italy). *Bull. Volcanol.* 74, 1859–1863. <https://doi.org/10.1007/s00445-012-0637-6>.
- Inguaggiato, S., Mazot, A., Diliberto, S., Inguaggiato, C., Madonia, P., Rouwet, D., Vita, F., 2012b. Total CO₂ output from Vulcano Island (Aeolian Islands, Italy). *Geochem. Geophys. Geosyst.* 13, 1–19. [https://doi.org/10.1029/2011GC003920\(Q2012\)](https://doi.org/10.1029/2011GC003920(Q2012)).
- Inguaggiato, S., Jácome Paz, M.P., Mazot, A., Delgado Granados, H., Inguaggiato, C., Vita, F., 2013. CO₂ output discharged from Stromboli Island (Italy). *Chem. Geol.* 339, 52–60. <https://doi.org/10.1016/j.chemgeo.2012.10.008>.
- Inguaggiato, C., Vita, F., Diliberto, S., Calderone, L., 2017. The role of the aquifer in soil CO₂ degassing in volcanic peripheral areas: a case study of Stromboli Island (Italy). *Chem. Geol.* 469, 110–116. <https://doi.org/10.1016/j.chemgeo.2016.12.017>.
- Italiano, F., Sasmaz, A., Yuce, G., Okan, O., 2013. Thermal fluids along the East Anatolian Fault Zone (EAZ): geochemical features and relationships with the tectonic setting. *Chem. Geol.* 339, 103–114.
- Italiano, F., Yuce, G., Uysal, I.T., Gasparon, M., Morelli, G., 2014. Insights into mantle-type volatiles contribution from the dissolved gases in artesian waters of the Great Artesian Basin, Australia. *Chem. Geol.* 378–379, 75–88.
- Italiano, F., Yuce, G., Di Bella, M., Rojat, B., Sabatino, G., Tripodo, A., Martelli, M., Rizzo, A.L., Misseri, M., 2017. Noble gases and rock geochemistry of alkaline intraplate volcanoes from the Amik and Ceyhan-Osmaniye areas, se Turkey. *Chem. Geol.* 469, 34–46.
- Jácome Paz, M.P., Inguaggiato, S., Taran, Y., 2016a. PCarbon dioxide emissions from Specchio di Venere Lake. *Bull. Volcanol.* 78, 29. <https://doi.org/10.1007/s00445-016-1023-6>.
- Jácome Paz, M.P., Taran, Y., Inguaggiato, S., Collard, N., 2016b. CO₂ flux and chemistry of El Chichón crater lake (México) in the period 2013–2015: Evidence for the enhanced volcano activity. *Geophys. Res. Lett.* 43, 127–134. <https://doi.org/10.1002/2015GL066354>.
- Jácome-Paz, M.P., Pérez-Zárate, D., Prol-Ledesma, R.M., Rodríguez-Díaz, A.A., Estrada-Murillo, A.M., González-Romo, I.A., Magaña-Torres, E., 2019. Two new geothermal prospects in the Mexican Volcanic Belt: La Escalera and Agua Caliente-Tzitzio geothermal springs, Michoacán, México. *Geothermics* 80, 44–55. <https://doi.org/10.1016/j.geothermics.2019.02.004>.
- Klusman, R.W., 1993. *Soil Gas and Related Methods for Natural Resource Exploration*. Wiley, New York.
- Kurz, W., Imber, J., Wibberley, A.J., Holdsworth, R.E., Collettini, C., Collettini, C., 2008. The internal structure of fault zones fluid flow and mechanical properties. In: Wibberley J., C.A., Kurz, W., Imber, J., Holdsworth, R.E. (Eds.), *The Internal Structure of Fault Zones: Implications for Mechanical and Fluid-Flow Properties*, pp. 1–3. [https://doi.org/10.1144/SP299.10305-8719/08/\\$15.00](https://doi.org/10.1144/SP299.10305-8719/08/$15.00).
- Lamberti, M.C., Vigide, N., Venturi, S., Agusto, M., Yakupsky, D., Winocur, D., Barcelona, H., Velez, M.L., Cardellini, C., Tassi, F., 2019. Structural architecture releasing deep-sourced carbon dioxide diffuse degassing at the Caviahue-Copahue Volcanic Complex. *J. Volcanol. Geotherm. Res.* 374, 131–141.
- Lombardi, S., Guerra, M., Etiöpe, G., 1996. The refinement of soil gas analysis as a geological investigative technique. 4th CEC R&D Programme on Management and Storage of Radioactive Waste (1990–1994).
- Matthews, M.D., 1985. Effects of hydrocarbon leakage on earth surface materials. In: Davidson, M.J. (Ed.), *Unconventional Methods in Exploration for Petroleum and Natural Gas*. IV. South. Methodist Univ. Press, Dallas, Tex, pp. 27–44.

- Mazot, A., Taran, Y., 2009. CO_2 flux from volcanic Lake of El Chichón (Méjico). *Geofis. Int.* 48 (1), 73–83.
- Morán-Zenteno, D.J., Cerca, M., Keppie, J.D., 2007. The Cenozoic tectonic and magmatic evolution of southwestern México: advances and problems of interpretation. In: Alaniz-Álvarez, S.A., Nieto-Samaniego, Á.F. (Eds.), *Geology of México: Celebrating the Centenary of the Geological Society of México: Geological Society of America Special Paper*. 422, pp. 71–91. [https://doi.org/10.1130/2007.2422\(03\)](https://doi.org/10.1130/2007.2422(03)).
- Notsu, K., Mori, T., Chanchah, D., Vale, S., Kagi, H., Ito, T., 2006. Monitoring quiescent volcanoes by diffuse CO_2 degassing: case study of Mt. Fuji, Japan. *Pure Appl. Geophys.* 163, 825–835.
- Pasquare, G., Ferrari, L., Garduño, V.H., Tibaldi, A., Vezzoli, L., 1991. *Geologic Map of the Central Sector of the Mexican Volcanic Belt, States of Guanajuato and Michoacán, Mexico*. The Geological Society of America, U.S. A., Boulder, Colorado.
- Pérez-Zárate, D., Jácome-Paz, M.P., Estrada-Murillo, A.M., Magaña-Torres, E., Prol-Ledesma, R.M., 2017. Medición de flujo de CO_2 y caracterización geoquímica de aguas termales en los sitios La Escalera y Agua Caliente, Michoacán. *Proceedings of the Annual Meeting of UGM, Puerto Vallarta, Jalisco, México*.
- Pfanz, H., Yuce, G., Gulbay, A.H., Gokgoz, A., 2019. Deadly CO_2 gases in the Plutonium of Hierapolis (Denizli, Turkey). *Archaeol. Anthropol. Sci.* 11 (4), 1359–1371. <https://doi.org/10.1007/s12520-018-0599-5>.
- Priest, S.D., 1993. *Discontinuity Analysis for Rock Engineering*. United Kingdom, Chapman & Hall, London, p. 473.
- Riedel, W., 1929. *Zur Mechanik Geologischer Brucherscheinungen*. Zentralblatt für Mineralogie, Geologie und Paläontologie B 354–368.
- Ring, U., Uysal, I.T., Yuce, G., Ünal-Imer, E., Italiano, F., Imer, A., Zhao, J., 2016. Recent mantle degassing recorded by carbonic spring deposits along sinistral strike-slip faults, south-central Australia. *Earth Planet. Sci. Lett.* 454, 304–318.
- Roberts, J.J., Wood, R.A., Wilkinson, M., Haszeldine, S., 2015. Surface controls on the characteristics of natural CO_2 seeps: implications for engineered CO_2 stores. *Geofluids* 15 (3), 453–463.
- Sibson, R.H., 2000. Fluid involvement in normal faulting. *J. Geodyn.* 29, 469–499.
- Sichel, H.S., 1966. The estimation of means and associated confidence limits for small samples from lognormal populations. *Proceedings Symposium a Mathematical Statistics and Computer Applications in Ore Valuation*. The South African Institute of Mining and Metallurgy, pp. 106–122.
- Sinclair, A.J., 1974. Selection of threshold values in geochemical data using probability graphs. *J. Geochem. Explor.* 3, 129–149.
- Sokolov, V.A., 1971. *Geochemistry of Natural Gases*. Niedra, Moscow.
- Tamburello, G., Pondrelli, S., Chiodini, G., Rouwet, D., 2018. Global-scale control of extensional tectonics on CO_2 earth degassing. *Nat. Commun.*, 4608 <https://doi.org/10.1038/s41467-018-07087>.
- Tukey, J.W., 1977. *Exploratory Data Analysis*. Addison-Wesley Longman, Boston.
- West Systems, 2012. “Portable Diffuse Flux Meter with LI-COR CO_2 Detector,” *Handbook*. West Systems srl, Italy.
- Wilks, S.S., 1932. Certain generalizations in the analysis of variance. *Biometrika* 471–494.
- Yaltırak, C., Yalcin, T., Yuce, G., Bozkurtoglu, E., 2005. Water level changes in shallow wells before and after the 1999 Izmit and Düzce earthquakes and comparison with long term water level observations (1999–2004), NW Turkey. *Turk. J. Earth Sci.* 14 (3), 1–29.
- Yuce, G., Taskiran, L., 2013. Isotope and chemical compositions of thermal fluids at Tekman Geothermal Area (Eastern Turkey). *Geochim. J.* 47 (4), 423–435.
- Yuce, A.G., Ugurluoglu, Y.D., 2003. Earthquake dates and water level changes in wells in the Eskisehir Region, Turkey (technical note). *Hydrol. Earth Syst. Sci.* 7 (5), 777–781.
- Yuce, G., Ugurluoglu, Y.D., Nadar, N., Yalcin, H.T., Yaltırak, C., Streil, T., Oeser, V., 2010. Monitoring of earthquake precursors by multi-parameter stations in Eskisehir Region (Turkey). *Appl. Geochem.* 25 (4), 572–579.
- Yuce, G., Italiano, F., D'Alessandro, W., Yalcin, T.H., Yasin, D.U., Gulbay, A.H., Ozyurt, N.N., Rojaj, B., Karabacak, V., Bellomo, S., Brusca, L., Yang, T., Fu, C.C., Lai, C.W., Ozacar, A., Walia, V., 2014. Origin and interactions of fluids circulating over the Amik Basin (Hatay-Turkey) and relationships with the hydrologic, geologic and tectonic settings. *Chem. Geol.* 388, 23–39.
- Yuce, G., Fu, C., D'Alessandro, W., Gulbay, A.H., Lai, C.W., Bellomo, S., Yang, T.F., Italiano, F., Walia, V., 2017a. Geochemical characteristics of soil radon and carbon dioxide within the Dead Sea Fault and Karasu Fault in the Amik Basin (Hatay), Turkey. *Chem. Geol.* 469, 129–146.
- Yuce, G., Italiano, F., Taskiran, L., Yasin, D., Gulbay, A.H., 2017b. Assessment of the origin and geothermal potential of the thermal waters by hydro-isotope geochemistry: Eskisehir province, Turkey. *Isotopes and Environmental Health Studies* 53 (2), 198–211.
- Zeeb, C., Gomez-Rivas, E., Bons, P.D., Blum, P., 2013. Evaluation of sampling methods for fracture network characterization using outcrops. *Bulletin of the Southwestern Association of Petroleum Geologists*, AAPG 97 (9), 1545–1566.
- Zhiguan, S., 1991. A study on the origin of fault gases in western Yunnan. *Earthquake Res. China* 5 (1), 45–52 (1991).